Dissolved iron in the North Atlantic Ocean and Labrador Sea along the GEOVIDE section (GEOTRACES section GA01)

Manon Tonnard[1,2,3], Hélène Planquette[1], Andrew R. Bowie[2,3], Pier van der Merwe[2], Morgane Gallinari[1], Floriane Desprez de Gésincourt[1], Yoan Germain[4], Arthur Gourain[5], Marion Benetti[6,7], Gilles Reverdin[7], Paul Tréguer[1], Julia Boutorh[1], Marie Cheize[1], François Lacan[8], Jan-Lukas Menzel Barraqueta[9,10], Leonardo Pereira-Contreira[11], Rachel Shelley[1,12,13], Pascale Lherminier[14], Géraldine Sarthou[1]

1Univ Brest, CNRS, IRD, Ifremer, LEMAR, F-29280 Plouzane, France

[2]Antarctic Climate and Ecosystems – Cooperative Research Centre, University of Tasmania, Hobart, TAS 7001, Australia

[3]Institute for Marine and Antarctic Studies, University of Tasmania, Hobart, TAS 7001, Australia

[4]Laboratoire Cycles Géochimiques et ressources – Ifremer, Plouzané, 29280, France

[5]Ocean Sciences Department, School of Environmental Sciences, University of Liverpool, L69 3GP, UK

[6]Institute of Earth Sciences, University of Iceland, Reykjavik, Iceland

[7]LOCEAN, Sorbonne Universités, UPMC/CNRS/IRD/MNHN, Paris, France

[8]LEGOS, Université de Toulouse - CNRS/IRD/CNES/UPS – Observatoire Midi-Pyrénées, Toulouse, France

[9]GEOMAR Helmholtz-Zentrum für Ozeanforschung Kiel Wischhofstraße 1-3, Geb. 12 D-24148 Kiel, Germany

[10]Department of Earth Sciences, Stellenbosch University, Stellenbosch, 7600, South Africa

[11]Fundação Universidade Federal do Rio Grande (FURG), R. Luis Loréa, Rio Grande –RS, 96200-350, Brazil

[12]Dept. Earth, Ocean and Atmospheric Science, Florida State University, 117 N Woodward Ave, Tallahassee, Florida, 32301, USA

[13]School of Geography, Earth and Environmental Sciences, University of Plymouth, Drake Circus, Plymouth, PL4 8AA, UK

[14] Ifremer, Univ Brest, CNRS, IRD, Laboratoire d'Océanographie Physique et Spatiale (LOPS), IUEM, F-29280, Plouzané, France

Correspondence to: geraldine.sarthou@univ-brest.fr; helene.planquette@univ-brest.fr

Abstract.

Dissolved Fe (DFe) samples from the GEOVIDE voyage (GEOTRACES GA01, May-June 2014) in the North Atlantic Ocean were analysed using a Sea*FAST*-pico[TM] coupled to an Element XR SF-ICP-MS and provided interesting insights on the Fe sources in this area. Overall, DFe concentrations ranged from 0.09 ± 0.01 nmol L^{-1} to 7.8 ± 0.5 nmol L^{-1}. Elevated DFe concentrations were observed above the Iberian, Greenland and Newfoundland Margins likely due to riverine inputs from the Tagus River, meteoric water inputs and sedimentary inputs. Deep winter convection occurring the previous winter provided iron-to-nitrate ratios sufficient to sustain phytoplankton growth and lead to relatively elevated DFe concentrations within subsurface waters of the Irminger Sea. Increasing DFe concentrations along the flow path of the Labrador Sea Water were attributed to sedimentary inputs from the Newfoundland Margin. Bottom waters from the Irminger Sea displayed high DFe concentrations likely due to the dissolution of Fe-rich particles in the Denmark Strait Overflow Water and the Polar Intermediate Water. Finally, the nepheloid layers located in the different basins and at the Iberian Margin were found to act as either a source or a sink of DFe depending on the nature of particles with organic particles likely releasing DFe and Mn-particles scavenging DFe.

1 Introduction

The North Atlantic Ocean is known for its pronounced spring phytoplankton blooms (Henson et al., 2009; Longhurst, 2007). Phytoplankton blooms induce the capture of aqueous carbon dioxide through photosynthesis, and conversion into particulate organic carbon (POC). This POC is then exported into deeper waters through sinking and ocean currents. Via these processes, and in conjunction with the physical carbon pump, the North Atlantic Ocean is the largest oceanic sink of anthropogenic CO_2 (Pérez et al., 2013), despite covering only 15% of global ocean area (Humphreys et al., 2016; Sabine et al., 2004) and is therefore crucial for Earth's climate.

Indeed, phytoplankton must obtain, besides light and inorganic carbon, chemical forms of essential elements, termed nutrients to be able to photosynthesise. The availability of these nutrients in the upper ocean frequently limits the activity and abundance of these organisms together with light conditions (Moore et al., 2013). In particular, winter nutrient reserves in surface waters set an upper limit for biomass accumulation during the annual spring-to-summer bloom and will influence the duration of the bloom (Follows and Dutkiewicz, 2001; Henson et al., 2009; Moore et al., 2013; 2008). Hence, nutrient depletion due to biological consumption is considered as a major factor in the decline of blooms (Harrison et al., 2013).

The extensive studies conducted in the North Atlantic Ocean through the Continuous Plankton Recorder (CPR) have highlighted the relationship between the strength of the westerlies and the displacement of the subarctic front (SAF), (which corresponds to the North Atlantic Oscillation (NAO) index (Bersch et al., 2007)), and the phytoplankton dynamics of the central North Atlantic Ocean (Barton et al., 2003). Therefore, the SAF not only delineates the subtropical gyre from the subpolar gyre but also two distinct systems in which phytoplankton limitations are controlled by different factors. In the North Atlantic Ocean, spring phytoplankton growth is largely light-limited within the subpolar gyre. Light levels are primarily set by freeze-thaw cycles of sea ice and the high-latitude extremes in the solar cycle (Longhurst, 2007). Simultaneously, intense winter mixing supplies surface waters with high concentrations of nutrients. In contrast, within the subtropical gyre, the spring phytoplankton growth is less impacted by the light regime and has been shown to be N and P-co-limited (e.g. Harrison et al., 2013; Moore et al., 2008). This is principally driven by Ekman downwelling with an associated export of nutrients out of the euphotic zone (Oschlies, 2002). Thus, depending on the location of the SAF, phytoplankton communities from the central North Atlantic Ocean will be primarily light or nutrient limited.

82

83 However, once the water column stratifies and phytoplankton are released from light limitation,
84 seasonal high-nutrient, low chlorophyll (HNLC) conditions were reported at the transition zone
85 between the gyres, especially in the Irminger Sea and Iceland Basin (Sanders et al., 2005). In these
86 HNLC zones, trace metals are most likely limiting the biological carbon pump. Among all the trace
87 metals, Fe has been recognized as the prime limiting element of North Atlantic primary productivity
88 (e.g. Boyd et al., 2000; Martin et al., 1994; 1988; 1990). Indeed, Fe is a key element for a number of
89 metabolic processes (e.g. Morel et al., 2008). However, the phytoplankton community has been
90 shown to become N and/or Fe-(co)-limited in the Iceland Basin and the Irminger Sea (e.g. Nielsdóttir
91 et al., 2009; Painter et al., 2014; Sanders et al., 2005).
92 In the North Atlantic Ocean, dissolved Fe (DFe) is delivered through multiple pathways such as ice-
93 melting (e.g. Klunder et al., 2012; Tovar-Sanchez et al., 2010), atmospheric inputs (Achterberg et al.,
94 2018; Baker et al., 2013; Shelley et al., 2015; 2017), coastal runoff (Rijkenberg et al., 2014), sediment
95 inputs (Hatta et al., 2015), hydrothermal inputs (Achterberg et al., 2018; Conway and John, 2014) and
96 by water mass circulation (vertical and lateral advections, e.g. Laes et al., 2003). Dissolved Fe can be
97 regenerated through biological recycling (microbial loop, zooplankton grazing, e.g. Boyd et al., 2010;
98 Sarthou et al., 2008). Iron is removed from the dissolved phase by biological uptake, export and
99 scavenging throughout the water column and precipitation (itself a function of salinity, pH of seawater
100 and ligand concentrations).
101 Although many studies investigated the distribution of DFe in the North Atlantic Ocean, much of this
102 work was restricted to the upper layers (< 1000 m depth) or to one basin. Therefore, uncertainties
103 remain on the large-scale distribution of DFe in the North Atlantic Ocean and more specifically within
104 the subpolar gyre where few studies have been undertaken, and even fewer in the Labrador Sea. In
105 this biogeochemically important area, high-resolution studies are still lacking for understanding the
106 processes influencing the cycle of DFe.
107 The aim of this paper is to elucidate the sources and sinks of DFe, its distribution regarding water
108 masses and assesses the links with biological activity along the GEOVIDE (GEOTRACES-GA01)
109 transect. This transect spanned several biogeochemical provinces including the West European
110 Basin, the Iceland Basin, the Irminger and the Labrador Seas (Fig. 1). In doing so we hope to
111 constrain the potential long-range transport of DFe through the Deep Western Boundary Current
112 (DWBC) via the investigation of the local processes effecting the DFe concentrations within the three

113   main water masses that constitute it: Iceland Scotland Overflow Water (ISOW), Denmark Strait

114   Overflow Water (DSOW) and Labrador Sea Water (LSW).

115

116   **2 Material and methods**

117

118   **2.1 Study area and sampling activities**

119   Samples were collected during the GEOVIDE (GEOTRACES-GA01 section, Fig. 1) oceanographic

120   voyage from 15 May 2014 (Lisbon, Portugal) to 30 June 2014 (St. John's, Newfoundland, Canada)

121   aboard N/O *Pourquoi Pas?*. The study was carried out along the OVIDE line (http://www.umr-

122   lops.fr/Projets/Projets-actifs/OVIDE, previously referred to as the WOCE A25 Greenland to Portugal

123   section), and in the Labrador Sea (corresponding to the WOCE A01 leg 3 Greenland to Newfoundland

124   section). The OVIDE line has been sampled every two years since 2002 in the North Atlantic (e.g.

125   Mercier et al., 2015), and in the Labrador Sea (broadly corresponding to the WOCE A01 leg 3

126   Greenland to Newfoundland section). In total, 32 stations were occupied, and samples were usually

127   collected at 22 depths, except at shallower stations close to the Iberian, Greenland and Canadian

128   shelves (Fig. 1) where fewer samples (between 6 and 11) were collected. To avoid ship contamination

129   of surface waters, the shallowest sampling depth was 15 m at all stations. Therefore, 'surface water

130   samples' refers to 15m depth.

131   Samples were collected using a trace metal clean polyurethane powder-coated aluminium frame

132   rosette (hereafter referred to as TMR) equipped with twenty-two 12L, externally closing, Teflon-lined,

133   GO-FLO bottles (General Oceanics) and attached to a Kevlar[®] line. The cleaning protocols for

134   sampling bottles and equipment followed the guidelines of the GEOTRACES Cookbook

135   (www.geotraces.org, Cutter et al., 2017). After TMR recovery, GO-FLO bottles were transferred into a

136   clean container equipped with a class 100 laminar flow hood. Samples were either taken from the

137   filtrate of particulate samples (collected on polyethersulfone filters, 0.45 µm supor[®], see Gourain et al.,

138   2019) or after filtration using 0.2 µm filter cartridges (Sartorius SARTOBRAN[®] 300) due to water

139   budget restriction (Table 1). Filtration techniques were not directly compared for the same samples,

140   however, Wilcoxon statistical tests were performed to compare the distribution of DFe at each pair of

141   adjacent stations where the change of filtration technique was performed (see Table 1). No significant

142   differences were observed (p-value > 0.2) for all pairs of stations (n = 9), except between stations

143   11/13 and 13/15. Moreover, both filtration techniques are deemed acceptable by the GEOTRACES

144   guidelines. Seawater was collected in acid-cleaned 60 mL LDPE bottles, after rinsing 3 times with
145   about 20 mL of seawater. Teflon® tubing used to connect the filter holders or cartridges to the GO-FLO
146   bottles were washed in an acid-bath (10% v/v HCl, Suprapur®, Merck) for at least 12 h and rinsed
147   three times with Ultra High Purity Water (UHPW > 18 MΩ.cm) prior to use. Samples were then
148   acidified to ~ pH 1.7 with HCl (Ultrapur® Merck, 2 ‰ v/v) under a class 100 laminar flow hood inside
149   the clean container. The sample bottles were then double bagged and stored at ambient temperature
150   in the dark before shore-based analyses one year after collection.
151   Large volumes of seawater sample (referred hereafter as the in-house standard seawater) were also
152   collected using a towed fish at around 2-3 m deep and filtered in-line inside a clean container through
153   a 0.2 µm pore size filter capsule (Sartorius SARTOBRAN® 300) and was stored unacidified in 20-30 L
154   LDPE carboys (Nalgene™). All the carboys were cleaned following the guidelines of the GEOTRACES
155   Cookbook (Cutter et al., 2017). This in-house standard seawater was used for calibration on the
156   SeaFAST-pico™ - SF-ICP-MS (see Section 2.2) and was acidified to ~ pH 1.7 with HCl (Ultrapur®
157   Merck, 2 ‰ v/v) at least 24h prior to analysis.
158
159   **2.2 DFe analysis with SeaFAST-pico™**
160   Seawater samples were preconcentrated using a SeaFAST-pico™ (ESI, Elemental Scientific, USA)
161   and the eluent was directly introduced via a PFA-ST nebulizer and a cyclonic spray chamber in an
162   Element XR Sector Field Inductively Coupled Plasma Mass Spectrometer (Element XR SF-ICP-MS,
163   Thermo Fisher Scientific Inc., Omaha, NE), following the protocol of Lagerström et al. (2013).
164   High-purity grade solutions and water (Milli-Q) were used to prepare the following reagents each day:
165   the acetic acid-ammonium acetate buffer ($CH3COO^-$ and $NH4^+$) was made of 140 mL acetic acid (>
166   99% NORMATOM® - VWR chemicals) and ammonium hydroxide (25%, Merck Suprapur®) in 500 mL
167   PTFE bottles and was adjusted to pH 6.0 ± 0.2 for the on-line pH adjustment of the samples. The
168   eluent was made of 1.4 M nitric acid (HNO_3, Merck Ultrapur®) in Milli-Q water by a 10-fold dilution and
169   spiked with 1 µg L^{-1} ^{115}In (SCP Science calibration standards) to allow for drift correction. Autosampler
170   and column rinsing solutions were made of HNO_3 2.5% (v/v) (Merck Suprapur®) in Milli-Q water. The
171   carrier solution driven by the syringe pumps to move the sample and buffer through the flow injection
172   system was made in the same way.

All reagents, standards, samples, and blanks were prepared in acid cleaned low density polyethylene (LDPE) or Teflon fluorinated ethylene propylene (FEP) bottles. Bottles were cleaned following the GEOTRACES protocol (Cutter et al., 2017).

Mixed element standard solution was prepared gravimetrically using high purity standards (Fe, Mn, Cd, Co, Zn, Cu, Pb; SCP Science calibration standards) in HNO_3 3% (v/v) (Merck Ultrapur®). The distribution of the trace metals other than Fe will be reported elsewhere (Planquette et al., in prep.). A six-point calibration curve was prepared by standard additions of the mixed element standard to our acidified in-house standard and ran at the beginning, the middle and the end of each analytical session. Each analytical session consisted of about fifty samples. Final concentrations of samples and procedural blanks were calculated from In-normalized data. Data were blank-corrected by subtracting an average acidified Milli-Q blank that were pre-concentrated on the Sea*FAST*-pico^{TM} in the same way as the samples and seawater standards. The errors associated to each sample were calculated as the standard deviation for five measurements of low-Fe seawater samples. The mean Milli-Q blank was equal to 0.08 ± 0.09 nmol L^{-1} (n = 17) considering all analytical sessions. The detection limit, calculated for a given run as three times the standard deviation of the Milli-Q blanks, was on average 0.05 ± 0.05 nmol L^{-1} (n = 17). Reproducibility was assessed through the standard deviation of replicate samples (every 10th sample was a replicate) and the average of the in-house standard seawater, and was equal to 17% (n = 84). Accuracy was determined from the analysis of consensus (SAFe S, GSP) and certified (NASS-7) seawater matrices (see Table 2) and in-house standard seawater (DFe = 0.42 ± 0.07 nmol L^{-1}, n = 84). Note that all the DFe values were generated in nmol kg^{-1} using the Sea*FAST*-pico^{TM} coupled to an Element XR SF-ICP-MS and were converted to nmol L^{-1} using the actual density (in kg L^{-1}) of each seawater sample (Table 1) to be directly comparable with literature.

2.3 Meteoric water and sea ice fraction calculation

We considered the different contributions of, Sea-Ice Melt (SIM), Meteoric Water (MW), and saline seawater, at Stations 53, 61 and 78 using the procedure and mass balance calculations that are fully described in Benetti et al. (2016). Briefly, we considered two types of seawater, namely Atlantic Water (AW) and Pacific Water (PW). The relative proportions of AW () and PW () are calculated based on the distinctive nitrogen to phosphorus (N-P) relationships for the two water masses (Jones et al., 1998) as follows (e.g. Sutherland et al., 2009):

$$f_{PW} = \frac{N^m - N^{AW}}{N^{PW} - N^{AW}} \text{ (eq.1)}$$

where is the measured dissolved inorganic nitrogen, and are the values for pure Atlantic and Pacific water estimated from Jones et al. (1998), respectively. and values are calculated by substituting the PO_4^m value in the equation of the pure AW and PW N-P lines from Jones et al. (1998). However, during GEOVIDE, the phosphate depleted near-surface values led to unrealistic lower than just below the subsurface. Therefore, for all surface samples, the estimates were replaced by the values at 100 m.. Then, the surface values were adjusted by a factor of dilution proportional to the sample salinity.

After estimating the relative proportions of AW () and PW () and their respective salinity and $\delta^{18}O$ affecting each samples, the contribution of SIM and MW can be determined using measured salinity (and $\delta^{18}O$ (). The mass balance calculations are presented below:

$$f_{AW} + f_{PW} + f_{MW} + f_{SIM} = 1 \text{ (eq.2)}$$

$$f_{AW} \cdot S_{AW} + f_{PW} \cdot S_{PW} + f_{MW} \cdot S_{MW} + f_{SIM} \cdot S_{SIM} = S_m \text{ (eq.3)}$$

$$f_{AW} \cdot \delta O_{AW}^{18} + f_{PW} \cdot \delta O_{PW}^{18} + f_{MW} \cdot \delta O_{MW}^{18} + f_{SIM} \cdot \delta O_{SIM}^{18} = \delta O_m^{18} \text{ (eq.4)}$$

where f_{AW}, f_{PW}, f_{MW}, f_{SIM} are the relative fraction of AW, PW, MW, and SIM. To calculate the relative fractions of AW, PW, MW and SIM we used the following end-members: = 35, = +0.18‰ (Benetti et al., 2016); = 32.5, = -1‰ (Cooper et al., 1997; Woodgate and Aagaard, 2005); = 0, = -18.4‰ (Cooper et al., 2008); = 4, = +0.5‰ (Melling and Moore, 1995).

Negative sea-ice fractions indicated a net brine release while positive sea-ice fractions indicated a net sea-ice melting. Note that for stations over the Greenland Shelf, we assumed that Pacific Water (PW) contribution was negligible for the calculations, supported by the very low PW fractions found at Cape Farewell in May 2014 (see Figure B1 in Benetti et al., 2017), while for station 78, located on the Newfoundland shelf, we used nutrient measurements to calculate the PW fractions, following the approach from Jones et al. (1998) (the data are published in Benetti et al., 2017).

2.4 Ancillary measurements and mixed layer depth determination

Potential temperature (θ), salinity (S), dissolved oxygen (O_2) and beam attenuation data were retrieved from the CTD sensors (CTD SBE911 equipped with a SBE-43) that were deployed on a stainless steel rosette.Salinity profiles were calibrated using 1228 samples taken from the GO-FLO bottles, leading to a precision of 0.002 psu. The O_2 data could not be directly calibrated with GO-FLO samples, due to a the sampling time being too long, so the calibrated O_2 profiles acquired by the classic CTD at the same station were used to calibrate the O_2 profiles of the TMR CTD, with a precision estimated at 3 µmol/kg. Nutrient and total Chlorophyll-*a* (TChl-*a*) samples were collected using the classic CTD at the same stations as for the TMR. We used the data from the stainless steel

234 rosette casts that were deployed immediately before or after our TMR casts. Pigments were separated
235 and quantified following an adaptation of the method described by van Heukelem and Thomas (2001)
236 and the analytical procedure used is described in Ras et al. (2008). The method adaptation allowed for
237 higher sensitivity in the analysis of low phytoplankton biomass waters (see Ras et al., 2008). Briefly,
238 frozen filters were extracted at -20°C in 3 mL of methanol (100%), sonicated and then clarified by
239 vacuum filtration through Whatman GF/F filters. The total extraction time was 2 hours. The extracts
240 were then analysed by HPLC with a complete Agilent Technologies system 1200 (comprising LC
241 Chemstation software, a degasser, a binary pump, a refrigerated autosampler, a column thermostat
242 and a diode array detector) when possible on the same day as extraction. The sample extracts were
243 premixed (1:1) with a tetrabutylammonium acetate (TBAA) buffer solution (28 nM) prior to injection in
244 the HPLC. The mobile phase was a mix between a solution (A) of TBAA 28 mM:methanol (30:70, v:v)
245 and a solution (B) of 100% methanol (i.e. the organic solvent) with varying proportions during analysis.
246 After elution, pigment concentrations (in mg m-3) were calculated according to Beer-Lambert's law
247 (i.e. A = εLC) from the peak areas with an internal standard correction (Vitamin E acetate, Sigma) and
248 an external standard calibration (DHI Water and Environment, Denmark). This method allowed the
249 detection of 23 phytoplankton pigments. The detection limits, defined as three times the signal:noise
250 ratio for a filtered volume of 1 L, was 0.0001 mg.m-3 for total chlorophyll-a (TChl-a) and its injection
251 precision was 0.91%
252 All these data are available on the LEFE/CYBER database (http://www.obs-
253 vlfr.fr/proof/php/geovide/geovide.php).
254 The mixed layer depth (Z_m) for each station was calculated using the function "calculate.mld" (part of
255 the "rcalcofi" package, Ed Weber at NOAA SWFSC) created by Sam McClathie (NOAA Federal, 30th
256 December 2013) for R software and where Z_m is defined as an absolute change in the density of
257 seawater at a given temperature ($\Delta\sigma_\theta \geq 0.125$ kg m^{-3}) with respect to an approximately uniform region
258 of density just below the ocean surface (Kara et al., 2000). In addition to the density criterion, the
259 temperature and salinity profiles were inspected at each station for uniformity within this layer. When
260 they were not uniform, the depth of any perturbation in the profile was chosen as the base of the Z_m
261 (Table 1).
262

2.5 Statistical analysis

All statistical approaches, namely the comparison between the pore size used for filtration, correlations and Principal Component Analysis (PCA), were performed using the R statistical software (R development Core Team 2012). For all the results, p-values were calculated against the threshold value alpha (α), that we assigned at 0.05, corresponding to a 95% level of confidence. For all data sets, non-normal distributions were observed according to the Shapiro-Wilk test. Therefore, the significance level was determined with a Wilcoxon test.

All sections and surface layer plots were prepared using Ocean Data View (Schlitzer, 2016).

2.6 Water mass determination and associated DFe concentrations

The water mass structure in the North Atlantic Ocean from the GEOVIDE voyage was quantitatively assessed by means of an extended Optimum Multi-Parameter (eOMP) analysis with 14 water masses (for details see García-Ibáñez et al., 2015; this issue). Using this water mass determination, DFe concentrations were considered as representative of a specific water mass only when the contribution of this specific water mass was higher than 60% of the total water mass pool.

2.7 Database

The complete database of dissolved Fe is available in the electronic supplement www.biogeosciences.net. Overall, 540 data points of dissolved Fe are reported, among which 511 values are used in this manuscript. The remaining 29 values (5.7% of the total dataset) are flagged as (suspect) outliers. These 29 outliers, flagged as "3" in the table, were not used in figures and in the interpretation of this manuscript . The criteria for rejection were based on the comparison with other parameters measured from the same GO-FLO sampler, and curve fitting versus samples collected above and below the suspect sample. The complete data set will be available in national and international databases (LEFE-CYBER, http://www.obs-vlfr.fr/proof/index2.php, and GEOTRACES http://www.bodc.ac.uk/geotraces/).

3 Results

3.1 Hydrography

The hydrology and circulation of the main water masses along the OVIDE section in the North Atlantic Subpolar Gyre and their contribution to the Atlantic Meridional Overturning Circulation (AMOC) have been described using an eOMP analysis by García-Ibáñez et al., (2015; 2018) and Zunino et al. (2017). For a schematic of water masses, currents and pathways, see Daniault et al. (2016). Hereafter we summarise the main features (Fig. 1 and 2).

Upper waters (~ 0 – 800 m) - The cyclonic circulation of Eastern North Atlantic Central Water (ENACW) ($12.3 < \theta < 16°C$, $35.66 < S < 36.2$, $241 < O_2 < 251$ µmol kg^{-1}) occupied the water column from 0 to ~ 800 m depth from stations 1 to 25 representing 60% of the water mass pool. The sharp Subarctic Front (between stations 26 and 29), caused by the northern branch of the North Atlantic Current (NAC) separated the cyclonic subpolar from the anticyclonic subtropical gyre domains at 50°N and 22.5°W. ENACW were also encountered to a lesser extent and only in surface waters (from 0 to ~ 100 m depth) between stations 29 and 34 (representing less than 40% of the water mass pool). West of the Subarctic Front, Iceland SubPolar Mode Water (IcSPMW, $7.07 < \theta < 8°C$, $35.16 < S < 35.23$, $280 < O_2 < 289$ µmol kg^{-1}) was encountered from stations 34-40 (accounting for more than 45% of the water mass pool from 0 to ~ 800 m depth) and Irminger SubPolar Mode Water (IrSPMW, $\theta \approx 5°C$, $S \approx 35.014$) from stations 42-44 (representing to 40% of the water mass pool from 0 to ~ 250 m depth) and stations 49 and 60 (accounting for 40% of the water mass pool down to 1300 m depth). IcSPMW was also observed within the Subtropical gyre (stations 11-26), subducted below ENACW up to1000 m depth. Stations 63 (> ~ 200 m depth) and 64 (from surface down to ~ 500 m depth) exhibited a contribution of the IrSPMW higher than 45%. Stations 44, 49 and 60, from the Irminger Sea, and 63 from the Labrador Sea were characterised by lower sea-surface salinity ranges (S = [34.636, 34.903], stations 63 and 60, respectively), likely due to ice melting and meteoric water inputs. Subarctic Intermediate Water (SAIW, $4.5 < \theta < 6.0°C$, $34.70 < S < 34.80$) contributed to more than 40% of the water mass pool in the Iceland Basin between the surface and ~ 400 m depth at stations 29 and 32 and throughout the water column of stations 53, 56 and 61 and from surface down to ~ 200 m depth at station 63. From stations 68 to 78 surface waters were characterized by a minimum of salinity and a maximum of oxygen (S = 34.91, $O_2 = 285$ µmol kg^{-1}, $\theta \approx 3°C$) and corresponded to the newly formed Labrador Sea Water (LSW). The LSW was also observed in surface waters of station 44 with a similar contribution than IrSPMW (~ 40%).

11

324

325 *Intermediate waters (~ 800 – 1400 m)* - Mediterranean Outflow Water (MOW), distinguishable from
326 surrounding Atlantic Water by its high salinity tongue (up to 36.2), a minimum of oxygen (O_2 = 210
327 µmol kg^{-1}) and relatively high temperatures (up to 11.7°C) was observed from station 1 to 21 between
328 800 and 1400 m depth at a neutral density ranging from 27.544 to 27.751 kg m^{-3} with the maximum
329 contribution to the whole water mass pool seen at station 1 (64 ± 6%). Its main core was located at ~
330 1200 m depth off the Iberian shelf from stations 1 to 11 and then gradually rising westward due to
331 mixing with LSW within the North Atlantic subtropical gyre and a contribution of this water mass
332 decreasing until station 21 down to 10-20%. LSW (27.763 < neutral density < 27.724 kg m^{-3}) was
333 sourced from SPMW after intense heat loss and led to its deep convection. During GEOVIDE, LSW
334 formed by deep convection the previous winter was found at several stations in the Labrador Sea (68,
335 69, 71 and 77). After convecting, LSW splits into three main branches with two main cores separated
336 by the Reykjanes Ridge (stations 1-32, West European and Iceland Basins; stations 40-60, Irminger
337 Sea), and the last one entering the West European Basin (Zunino et al., 2017).

338

339 *Overflows and Deep waters (~ 1400 - 5500 m)* - North East Atlantic Deep Water (NEADW, 1.98 < θ <
340 2.50°C, 34.895 < S < 34.940) was the dominant water mass in the West European Basin at stations 1-
341 29 from 2000 m depth to the bottom and is characterized by high silicic acid (42 ± 4 µmol L^{-1}), nitrate
342 (21.9 ± 1.5 µmol L^{-1}) concentrations and lower oxygen concentration (O_2 ≈ 252 µmol kg^{-1}) (see
343 Sarthou et al., 2018). The core of the NEADW (stations 1-13) was located near the seafloor and
344 gradually decreased westward. Polar Intermediate Water (PIW, θ ≈ 0°C, S ≈ 34.65) is a ventilated,
345 dense, low-salinity water intrusion to the deep overflows within the Irminger and Labrador Seas that is
346 formed at the Greenland shelf. PIW represents only a small contribution to the whole water mass pool
347 (up to 27%) and was observed over the Greenland slope at stations 53 and 61 as well as in surface
348 waters from station 63 (from 0 to ~ 200 m depth), in intermediate waters of stations 49, 60 and 63
349 (from ~ 500 to ~ 1500 m depth) and in bottom waters of stations 44, 68, 69, 71 and 77 with a
350 contribution higher than 10%. Iceland Scotland Overflow Water (ISOW, θ ≈ 2.6°C, S ≈ 34.98) is partly
351 formed within the Arctic Ocean by convection of the modified Atlantic water. ISOW comes from the
352 Iceland-Scotland sills and flows southward towards the Charlie-Gibbs Fracture Zone (CGFZ) and
353 Bight Fracture Zone (BFZ) (stations 34 and 36) after which it reverses its flowing path northward and
354 enters the Irminger Sea (stations 40 and 42) to finally reach the Labrador Sea close to the Greenland

coast (station 49, station 44 being located in between this two opposite flow paths). Along the eastern (stations 26-36) and western (stations 40-44) flanks of the Reykjanes Ridge, ISOW had a contribution higher than 50% to the water mass pool. ISOW was observed from 1500 m depth to the bottom of the entire Iceland Basin (stations 29-38) and from 1800 to 3000 m depth within the Irminger Sea (stations 40-60). ISOW, despite having a fraction lower than 45% above the Reykjanes Ridge (station 38), was the main contributor to the water mass pool from 1300 m depth down to the bottom. ISOW was also observed within the Labrador Sea from stations 68 to 77. Finally, the deepest part of the Irminger (stations 42 and 44) and Labrador (stations 68-71) Seas were occupied by Denmark Strait Overflow Water (DSOW, $\theta \approx 1.30°C$, $S \approx 34.905$).

3.2 Ancillary data

3.2.1 Nitrate

Surface nitrate (NO_3^-) concentrations (García-Ibáñez et al., 2018; Pérez et al., 2018; Sarthou et al., 2018) ranged from 0.01 to 10.1 µmol L^{-1} (stations 53 and 63, respectively). There was considerable spatial variability in NO_3^- surface distributions with high concentrations found in the Iceland Basin and Irminger Sea (higher than 6 µmol L^{-1}), as well as at stations 63 (10.1 µmol L^{-1}) and 64 (5.1 µmol L^{-1}), and low concentrations observed in the West European Basin, in the Labrador Sea and above continental margins. The low surface concentrations in the West European Basin ranged from 0.02 (station 11) to 3.9 (station 25) µmol L^{-1}. Station 26 delineating the extreme western boundary of the West European Basin exhibited enhanced NO_3^- concentrations as a result of mixing between ENACW and IcSPMW, although these surface waters were dominated by ENACW. In the Labrador Sea (stations 68-78) low surface concentrations were observed with values ranging from 0.04 (station 68) to 1.8 (station 71) µmol L^{-1}. At depth, the lowest concentrations (lower than 15.9 µmol L^{-1}) were measured in ENACW (~ 0 - 800 m depth) and DSOW (> 1400 m depth), while the highest concentrations were measured within NEADW (up to 23.5 µmol L^{-1}), and in the mesopelagic zone of the West European and Iceland Basins (higher than 18.4 µmol L^{-1}).

13

384 **3.2.2 Chlorophyll-*a***

385 Overall, most of the phytoplankton biomass was localised above 100 m depth with lower total
386 chlorophyll-*a* (TChl-*a*) concentrations South of the Subarctic Front and higher at higher latitudes (see
387 supplementary material Fig. S1). While comparing TChl-*a* maxima considering all stations, the lowest
388 value (0.35 mg m^{-3}) was measured within the West European Basin (station 19, 50 m depth) while the
389 highest values were measured at the Greenland (up to 4.9 mg m^{-3}, 30 m depth, station 53 and up to
390 6.6 mg m^{-3}, 23 m depth, station 61) and Newfoundland (up to 9.6 mg m^{-3}, 30 m depth, station 78)
391 margins.

392

393 **3.3 Dissolved Fe concentrations**

394 Dissolved Fe concentrations (see supplementary material Table S1) ranged from 0.09 ± 0.01 nmol L^{-1}
395 (station 19, 20 m depth) to 7.8 ± 0.5 nmol L^{-1} (station 78, 371 m depth) (see Fig. 3). Generally, vertical
396 profiles of DFe for stations above the margins (2, 4, 53, 56, 61, and 78) showed an increase with
397 depth, although sea-surface maxima were observed at stations 2, 4 and 56. For these margin stations,
398 values ranged from 0.7 to 1.0 nmol L^{-1} in the surface waters. Concentrations increased towards the
399 bottom, with more than 7.8 nmol L^{-1} measured at station 78, approximately 1-3 nmol L^{-1} for stations 2,
400 4, 53, and 61, and just above 0.4 nmol L^{-1} for station 56 (Fig. 4). Considering the four oceanic basins,
401 mean vertical profiles (supplementary material Fig. S2) showed increasing DFe concentrations down
402 to 3000 m depth followed by decreasing DFe concentrations down to the bottom. Among deep-water
403 masses, the lowest DFe concentrations were measured in the West European Basin. The Irminger
404 Sea displayed the highest DFe concentrations from 1000 m depth to the bottom relative to other
405 basins at similar depths (Fig. 3 and supplementary material Fig. S2). In the Labrador Sea, DFe
406 concentrations were low and relatively constant at about 0.87 ± 0.06 nmol L^{-1} from 250 m to 3000 m
407 depth (Fig. S2). Overall, surface DFe concentrations were higher (0.36 ± 0.18 nmol L^{-1}) in the North
408 Atlantic Subpolar gyre (above 52°N) than in the North Atlantic Subtropical gyre (0.17 ± 0.05 nmol L^{-1}).
409 The surface DFe concentrations were generally smaller than 0.3 nmol L^{-1}, except for few stations in
410 the Iceland Basin (stations 32 and 38), Irminger (stations 40 and 42) and Labrador (station 63) Seas,
411 where values ranged between 0.4-0.5 nmol L^{-1}.

412

413 **3.4 DFe signatures in water masses**

414   In the Labrador Sea, IrSPMW exhibited an average DFe concentration of 0.61 ± 0.21 nmol L^{-1} (n=14).

415   DFe concentrations in the LSW were the lowest in this basin, with an average value of 0.71 ± 0.27

416   nmol L^{-1} (n=53) (see supplementary material Fig. S3). Deeper, ISOW displayed slightly higher average

417   DFe concentrations (0.82 ± 0.05 nmol L^{-1}, n=2). Finally, DSOW had the lowest average (0.68 ± 0.06

418   nmol L^{-1}, n=3, see supplementary material Fig. S3) and median (0.65 nmol L^{-1}) DFe values for

419   intermediate and deep waters.

420   In the Irminger Sea, surface waters were composed of SAIW (0.56 ± 0.24 nmol L^{-1}, n=4) and IrSPMW

421   (0.72 ± 0.32 nmol L^{-1}, n=34). The highest open-ocean DFe concentrations (up to 2.5 ± 0.3 nmol L^{-1},

422   station 44, 2600 m depth) were measured within this basin. In the upper intermediate waters, LSW

423   was identified only at stations 40 to 44, and had the highest DFe values with an average of 1.2 ± 0.3

424   nmol L^{-1} (n=14). ISOW showed higher DFe concentrations than in the Iceland Basin (1.3 ± 0.2 nmol L^{-1},

425   n=4). At the bottom, DSOW was mainly located at stations 42 and 44 and presented the highest

426   average DFe values (1.4 ± 0.4 nmol L^{-1}, n=5) as well as the highest variability from all the water

427   masses presented in this section (see supplementary material Fig. S3).

428   In the Iceland Basin, SAIW and IcSPMW displayed similar averaged DFe concentrations (0.67 ± 0.30

429   nmol L^{-1}, n=7 and 0.55 ± 0.34 nmol L^{-1}, n=22, respectively). Averaged DFe concentrations were similar

430   in both LSW and ISOW, and higher than in SAIW and IcSPMW (0.96 ± 0.22 nmol L^{-1}, n=21 and 1.0 ±

431   0.3 nmol L^{-1}, n=10, respectively, see supplementary material Fig. S3).

432   Finally, in the West European Basin, DFe concentrations in ENACW were the lowest of the whole

433   section with an average value of 0.30 ± 0.16 nmol L^{-1} (n=64). MOW was present deeper in the water

434   column but was not characterized by particularly high or low DFe concentrations relative to the

435   surrounding Atlantic waters (see supplementary material Fig. S3). The median DFe value in MOW

436   was very similar to the median value when considering all water masses (0.75 and 0.77 nmol L^{-1},

437   respectively, Fig. S3). LSW and IcSPMW displayed slightly elevated DFe concentrations compared to

438   the overall median with mean values of 0.82 ± 0.08 (n=28) and 0.80 ± 0.04 (n=8) nmol L^{-1},

439   respectively. The DFe concentrations in NEADW were relatively similar to the DFe median value of

440   the GEOVIDE voyage (0.71 and 0.77 nmol L^{-1}, respectively, Fig. S3.

441

442

443   **4 Discussion**

444

15

445　In the following sections, we will first discuss the high DFe concentrations observed throughout the
446　water column of stations 1 and 17 located in the West European Basin (Section 4.1), then, the
447　relationship between water masses and the DFe concentrations (Section 4.2) in intermediate (Section
448　4.2.2 and 4.2.3) and deep (Section 4.2.4 and 4.2.5) waters. We will also discuss the role of wind
449　(Section 4.2.1), rivers (Section 4.3.1), meteoric water and sea-ice processes (Section 4.3.2),
450　atmospheric deposition (Section 4.3.3) and sediments (Section 4.4) in delivering DFe. Finally, we will
451　discuss the potential Fe limitation using DFe:NO_3^- ratios (Section 4.5).

452

453

454　**4.1 High DFe concentrations at station 1 and 17**
455　Considering the entire section, two stations (stations 1 and 17) showed irregularly high DFe
456　concentrations (> 1 nmol L^{-1}) throughout the water column, thus suggesting analytical issues.
457　However, these two stations were analysed twice and provided similar results, therefore discarding
458　any analytical issues. This means that these high values originated either from genuine processes or
459　from contamination issues. If there had been contamination issues, one would expect a more random
460　distribution of DFe concentrations and less consistence throughout the water column. It thus appears
461　that contamination issues were unlikely to happen. Similarly, the influence of water masses to explain
462　these distributions was discarded as the observed high homogenized DFe concentrations were
463　restricted to these two stations. Station 1, located at the continental shelf-break of the Iberian Margin,
464　also showed enhanced PFe concentrations from lithogenic origin suggesting a margin source
465　(Gourain et al., 2019). Conversely, no relationship was observed between DFe and PFe nor
466　transmissometry for station 17. However, Ferron et al. (2016) reported a strong dissipation rate at the
467　Azores-Biscay Rise (station 17) due to internal waves. The associated vertical energy fluxes could
468　explain the homogenized profile of DFe at station 17, although such waves are not clearly evidenced
469　in the velocity profiles. Consequently, the elevated DFe concentrations observed at station 17 remain
470　unsolved.

471

472

473　**4.2 DFe and hydrology keypoints**

474

4.2.1 How do Air-sea interactions affect DFe concentration in the Irminger Sea?

Among the four distinct basins described in this paper, the Irminger Sea exhibited the highest DFe concentrations within the surface waters (from 0 to 250 m depth) with values ranging from 0.23 to 1.3 nmol L^{-1} for open-ocean stations. Conversely, low DFe concentrations were previously reported in the central Irminger Sea by Rijkenberg et al. (2014) (April-May, 2010) and Achterberg et al. (2018) (April-May and July-August, 2010) with DFe concentrations ranging from 0.11 to 0.15 and from ~ 0 to 0.14 nmol L^{-1}, respectively (see supplementary material Fig. S4 and Table S2). Differences might be due to the phytoplankton bloom advancement, the high remineralization rate (Lemaître et al., 2017) observed within the LSW in the Irminger Sea (see Section 4.1.3) and a deeper winter convection in early 2014. Indeed, enhanced surface DFe concentrations measured during GEOVIDE in the Irminger Sea could be due to intense wind forcing events that would deepen the winter Z_m down to the core of the Fe-rich LSW.

In the North Atlantic Ocean, the warm and salty water masses of the upper limb of the MOC are progressively cooled and become denser, and subduct into the abyssal ocean. In some areas of the SubPolar North Atlantic, deep convective winter mixing provides a rare connection between surface and deep waters of the MOC thus constituting an important mechanism in supplying nutrients to the surface ocean (de Jong et al., 2012; Louanchi and Najjar, 2001). Deep convective winter mixing is triggered by the effect of wind and a pre-conditioning of the ocean in such a way that the inherent stability of the ocean is minimal. Pickart et al. (2003) demonstrated that these conditions are satisfied in the Irminger Sea with the presence of weakly stratified surface water, a close cyclonic circulation, which leads to the shoaling of the thermocline and intense winter air-sea buoyancy fluxes (Marshall and Schott, 1999). Moore (2003) and Piron et al. (2016) described low-altitude westerly jets centred northeast of Cape Farewell, over the Irminger Sea, known as tip jet events. These events occur when wind is split around the orographic features of Cape Farewell, and are strong enough to induce deep convective mixing (Bacon et al., 2003; Pickart et al., 2003). It has also been shown that during winters with a positive North Atlantic Oscillation (NAO) index, the occurrence of such events is favoured (Moore, 2003; Pickart et al., 2003), which was the case in the winter 2013-2014, preceding the GEOVIDE voyage as opposed to previous studies (Lherminier, pers. comm.). The winter mixed layer depth prior to the cruise reached up to 1200 m depth in the Irminger Sea (Zunino et al., 2017), which was most likely attributed to a final deepening due to wind forcing events (centred at station 44). Such

17

505 winter entrainment was likely the process involved in the vertical supply of DFe within surface waters

506 fuelling the spring phytoplankton bloom with DFe values close to those found in LSW.

507

508 **4.2.2 Why don't we see a DFe signature in the Mediterranean Overflow Water (MOW)?**

509 On its northern shores, the Mediterranean Sea is bordered by industrialized European countries,

510 which act as a continuous source of anthropogenic derived constituents into the atmosphere, and on

511 the southern shores by the arid and desert regions of north African and Arabian Desert belts, which

512 act as sources of crustal material in the form of dust pulses (Chester et al., 1993; Guerzoni et al.,

513 1999; Martin et al., 1989). During the summer, when thermal stratification occurs, DFe concentrations

514 in the SML can increase over the whole Mediterranean Sea by 1.6-5.3 nmol L^{-1} in response to the

515 accumulation of atmospheric Fe from both anthropogenic and natural origins (Bonnet and Guieu,

516 2004; Guieu et al., 2010; Sarthou and Jeandel, 2001). After atmospheric deposition, the fate of Fe will

517 depend on the nature of aerosols, Fe-ligand binding capacity, vertical mixing, biological uptake, and

518 scavenging processes (Bonnet and Guieu, 2006; Wuttig et al., 2013). During GEOVIDE, MOW was

519 observed at percentages higher than ~ 60% from stations 1 to 13 between 900 and 1100 m depth and

520 associated with high dissolved aluminium (DAl, Menzel Barraqueta et al., 2018) concentrations (up to

521 38.7 nmol L^{-1}), confirming the high atmospheric deposition in the Mediterranean region. In contrast to

522 Al, no DFe signature was associated with MOW (Figs. 2 and 3). Using L-ADCP data during the cruise,

523 we estimated a translation velocity for the MOW of ~ 3-8 cm s-1, consistent with previous published

524 values (e.g. Armi et al., 1989; Schmidt et al., 1996). Our station 13 was located ~ 2000 km far from the

525 origin of the MOW, which would mean a transit time of ~ 1-2 years. This transit time would allow the

526 Fe signal to be preserved, when DFe residence times range from weeks to months in the surface

527 waters and from tens to hundreds of years in deep waters (de Baar and de Jong, 2001; Sarthou et al.,

528 2003; Croot et al., 2004; Bergquist and Boyle 2006; Gerringa et al 2015; Tagliabue et al., 2016). This

529 feature was also reported in some studies (Hatta et al., 2015; Thuróczy et al., 2010), while others

530 measured higher DFe concentrations in MOW (Gerringa et al., 2017; Sarthou et al., 2007). However,

531 MOW coincides with the maximum Apparent Oxygen Utilization (AOU) and it is not possible to

532 distinguish the MOW signal from the remineralisation signal (Sarthou et al., 2007). On the other hand,

533 differences between studies are likely originating from the intensity of atmospheric deposition and the

534 nature of aerosols. Indeed, Wagener et al. (2010) highlighted that large dust deposition events can

535 accelerate the export of Fe from the water column through scavenging. As a result, in seawater with

536 high DFe concentrations and where high dust deposition occurs, a strong individual dust deposition
537 event could act as a sink for DFe. It thus becomes less evident to observe a systematic high DFe
538 signature in MOW despite dust inputs.
539
540 **4.2.3 Fe enrichment in Labrador Sea Water (LSW)**
541 As described in Section 3.1, the LSW exhibited increasing DFe concentrations from its source area,
542 the Labrador Sea, toward the other basins with the highest DFe concentrations observed within the
543 Irminger Sea, suggesting that the water mass was enriched in DFe either locally in each basin or
544 during its flow path (see supplementary material Fig. S3). These DFe sources could originate from a
545 combination of high export of PFe and its remineralisation in the mesopelagic area and/or the
546 dissolution of sediment.
547 The Irminger and Labrador Seas exhibited the highest averaged integrated TChl-a concentrations (98
548 ± 32 mg m^{-2} and 59 ± 42 mg m^{-2}) compared to the West European and Iceland Basins (39 ± 10 mg m^{-2}
549 and 53 ± 16 mg m^{-2}), when the influence of margins was discarded. Stations located in the Irminger
550 (stations 40-56) and Labrador (stations 63-77) Seas, were largely dominated by diatoms (>50% of
551 phytoplankton abundances) and displayed the highest chlorophillide-*a* concentrations, a tracer of
552 senescent diatom cells, likely reflecting post-bloom condition (Tonnard et al., in prep.). This is in line
553 with the highest POC export data reported by Lemaitre et al. (2018) in these two oceanic basins. This
554 likely suggests that biogenic PFe export was also higher in the Labrador and Irminger Seas than in the
555 West European and Iceland Basins. In addition, Gourain et al. (2019) highlighted a higher biogenic
556 contribution for particles located in the Irminger and Labrador Seas with relatively high PFe:PAl ratios
557 (0.44 ± 0.12 mol:mol and 0.38 ± 0.10 mol:mol, respectively) compared to particles from the West
558 European and Iceland Basins (0.22 ± 0.10 and 0.38 ± 0.14 mol:mol, respectively, see Fig. 6A in
559 Gourain et al., 2019). However, they reported no difference in PFe concentrations between the four
560 oceanic basins, when the influence of margins was discarded, which likely highlighted the
561 remineralisation of PFe within the Irminger and Labrador Seas. Indeed, Lemaître et al. (2017) reported
562 higher remineralisation rates within the Labrador (up to 13 mmol C m^{-2} d^{-1}) and Irminger Seas (up to
563 10 mmol C m^{-2} d^{-1}) using the excess barium proxy (Dehairs et al., 1997), compared to the West
564 European and Iceland Basins (ranging from 4 to 6 mmol C m^{-2} d^{-1}). Therefore, the intense
565 remineralisation rates measured in the Irminger and Labrador Seas likely resulted in enhanced DFe
566 concentrations within LSW.

567   Higher DFe concentrations were, however, measured in the Irminger Sea compared to the Labrador

568   Sea and coincided with lower transmissometry values (i.e. 98.0-98.5% vs. >99%), thus suggesting a

569   particle load of the LSW. This could be explained by the reductive dissolution of Newfoundland Margin

570   sediments. Indeed, Lambelet et al. (2016) reported high dissolved neodymium (Nd) concentrations (up

571   to 18.5 pmol.kg^{-1}) within the LSW at the edge of the Newfoundland Margin (45.73°W, 51.82°N) as well

572   as slightly lower Nd isotopic ratio values relative to those observed in the Irminger Sea. They

573   suggested that this water mass had been in contact with sediments approximately within the last 30

574   years (Charette et al., 2015). Similarly, during GA03, Hatta et al. (2015) attributed the high DFe

575   concentrations in the LSW to continental margin sediments. Consequently, it is also possible that the

576   elevated DFe concentrations from the three LSW branches which entered the West European and

577   Iceland Basins and Irminger Sea was supplied through sediment dissolution (Measures et al., 2013)

578   along the LSW pathway.

579   The enhanced DFe concentrations measured in the Irminger Sea and within the LSW were thus likely

580   attributed to the combination of higher productivity, POC export and remineralisation as well as a DFe

581   supply from reductive dissolution of Newfoundland sediments to the LSW along its flow path. Using

582   temperature and salinity anomalies, Yashayaev et al. (2007) showed that the LSW reached the

583   Irminger Sea and the Iceland Basin in 1-2 years and 4-5 years, respectively, after its formation in the

584   Labrador Sea. The LSW transit time in this region is thus compatible with a DFe residence times (see

585   above).   **4.2.4 Enhanced DFe concentrations in the Irminger Sea bottom water**

586   Bottom waters from the Irminger Sea exhibited the highest DFe concentrations from the whole section,

587   excluding the stations at the margins. Such a feature could be due to i) vertical diffusion from local

588   sediment, ii) lateral advection of water mass(es) displaying enhanced DFe concentrations, and iii)

589   local dissolution of Fe from particles. Hereafter, we discuss the plausibility of these three hypotheses.

590   The GEOTRACES GA02 voyage (leg 1, 64PE319) which occurred in April-May 2010 from Iceland to

591   Bermuda sampled two stations north and south of our station 44 (~ 38.95°W, 59.62°N): station 5 (~

592   37.91°W, 60.43°N) and 6 (~ 39.71°W, 58.60°N), respectively. High DFe concentrations in samples

593   collected close to the bottom were also observed and attributed to sediment inputs highlighting

594   boundary exchange between seawater and surface sediment (Lambelet et al., 2016; Rijkenberg et al.,

595   2014). However, because a decrease in DFe concentrations was observed at our station 44 from 2500

596   m depth down to the bottom (Fig. 3 and Table S1), it appeared to be unlikely that these high DFe

597 concentrations will be the result of local sediment inputs, as no DFe gradient from the deepest
598 samples to those above was observed.

599 Looking at salinity versus depth for these three stations, one can observe the intrusion of Polar
600 Intermediate Water (PIW) at station 44 during GEOVIDE, which was not observed during the GA02
601 voyage and which contributed to about 14% of the water mass composition (García-Ibáñez et al.,
602 2018) and might therefore be responsible for the high DFe concentrations (see supplementary
603 material Fig. S5A). On the other hand, the PIW was also observed at station 49 (from 390 to 1240 m
604 depth), 60 (from 440 to 1290 m depth), 63 (from 20 to 1540 m depth), 68 (3340 m depth), 69 (from
605 3200 to 3440 m depth), 71 (from 2950 to 3440 m depth) and 77 (60 and 2500 m depth) with similar or
606 higher contributions of the PIW without such high DFe concentrations (maximum DFe = 1.3 ± 0.1 nmol
607 L^{-1}, 1240 m depth at station 49). At this station, the DSOW relative abundance was more than 20%
608 (Supp. Fig. S5). The overflow of this dense water in the Irminger Sea is associated with intense
609 cyclonic boluses (Käse et al. 2003) and the entrainment of waters from the Greenland margin and
610 slope by pulses of DSOW occurs all along its transport from Denmark Strait to the Greenland tip
611 (Magaldi et al., 2011; von Appen et al., 2014). This phenomenon may enrich the DSOW with Fe as
612 well as other elements. This was also observed for radium and actinium with a deviation from the
613 conservative behaviour of 226Ra (Le Roy et al., 2018) and an increase of 227Ac activity at station 44
614 at 2500 m, reflecting inputs of these tracers. Therefore, the high DFe concentrations observed in the
615 Irminger Sea might be inferred from substantial load of Fe-rich particles when DSOW is in contact with
616 the Greenland margin.

617

618 **4.2.5 Reykjanes Ridge: Hydrothermal inputs or Fe-rich seawater?**

619 Hydrothermal activity was assessed over the Mid Atlantic Ridge, namely the Reykjanes Ridge (RR),
620 from stations 36 to 40. Indeed, within the interridge database (http://www.interridge.org), the
621 Reykjanes Ridge is reported to have active hydrothermal sites. The sites were either confirmed (Baker
622 and German, 2004; German et al., 1994; Olaffson et al., 1991; Palmer et al., 1995) close to Iceland or
623 inferred (e.g. Chen, 2003; Crane et al., 1997; German et al., 1994; Sinha et al., 1997; Smallwood and
624 White, 1998) closer to the GEOVIDE section as no plume was detected but a high backscatter was
625 reported potentially corresponding to a lava flow. Therefore, hydrothermal activity at the sampling sites
626 remains unclear with no elevated DFe concentrations nor temperature anomaly above the ridge
627 (station 38). However, enhanced DFe concentrations (up to 1.5 ± 0.22 nmol L^{-1}, station 36, 2200 m

21

depth) were measured east of the Reykjanes Ridge (Fig. 3). This could be due to hydrothermal activity and resuspension of sunken particles at sites located North of the section and transported through ISOW towards the section (Fig. 3). Indeed, Achterberg et al. (2018) highlighted at ~60°N and over the Reykjanes Ridge a southward lateral transport of an Fe plume of up to 250-300 km. In agreement with these observations, previous studies (e.g. Fagel et al., 1996; Fagel et al., 2001; Lackschewitz et al., 1996; Parra et al., 1985) reported marine sediment mineral clays in the Iceland Basin largely dominated by smectite (> 60%), a tracer of hydrothermal alteration of basaltic volcanic materials (Fagel et al., 2001; Tréguer and De La Rocha, 2013). Kanzow and Zenk (2014) investigated the fluctuations of the ISOW plume around RR. The transit time, west of RR, between 60°N and the Bight Fracture Zone (BFZ) was around 5 months, compatible with the residence time of DFe (see above). Hence, the high DFe concentrations measured east of RR could be due to a hydrothermal source and/or the resuspension of (basaltic) particles and their subsequent dissolution.

West of the Reykjanes Ridge, a DFe-enrichment was also observed in ISOW at station 40 within the Irminger Sea (Fig. 3). The low transmissometer values within ISOW in the Irminger Sea (station 44) compared to the Iceland Basin (station 32) suggested a higher particle load (Fig. 4A in Gourain et al., 2019). These particles could come from the Bight Fracture Zone (BFZ, 56.91°N and 32.74°W) (Fig. 1) (Lackschewitz et al., 1996; Zou et al., 2017) since the transit time of the ISOW between BFZ and our station 40 is around 3 months (Kanzow and Zenk, 2014)..

4.3 What are the main sources of DFe in surface waters?

During GEOVIDE, enhanced DFe surface concentrations were observed at several stations (stations 1-4, 53, 61, 78) highlighting an external source of Fe to surface waters. The main sources able to deliver DFe to surface waters are riverine inputs, glacial inputs and atmospheric deposition. In the following sections, these potential sources of DFe to surface waters will be discussed.

4.3.1 Tagus riverine inputs

Enhanced DFe surface concentrations (up to 1.07 ± 0.12 nmol L^{-1}) were measured over the Iberian Margin (stations 1-4) and coincided with salinity minima (~ <35) and enhanced DAl concentrations (up to 31.8 nmol L^{-1}, Menzel Barraqueta et al., 2018). DFe and DAl concentrations were both significantly negatively correlated with salinity (R^2 = ~1 and 0.94, respectively) from stations 1 to 13 (Fig. 5).

659 Salinity profiles from station 1 to 4 showed evidence of a freshwater source with surface salinity
660 ranging from 34.95 (station 1) to 35.03 (station 4). Within this area, only two freshwater sources were
661 possible: 1) wet atmospheric deposition (4 rain events, Shelley, pers. comm.) and 2) the Tagus River,
662 since the ship SADCP data revealed a northward circulation with a velocity of around 0.1 m/s (P.
663 Lherminier and P. Zunino, Ifremer Brest, pers. comm.). The transit time from the estuary to our
664 stations above the shelf is around 15 days (150 km), which is short enough to preserve the DFe
665 signal. Our SML DFe inventories were about three times higher at station 1 ($\sim$ 1 nmol L^{-1}) than those
666 calculated during the GA03 voyage ($\sim$ 0.3 nmol L^{-1}, station 1). Atmospheric deposition were about one
667 order of magnitude higher during GA03 than during GA01 (Shelley et al., 2018; Shelley et al., 2015),
668 thus the atmospheric source seemed to be minor during GA01. Consequently, the Tagus River
669 appears as the most likely source responsible for these enhanced DFe concentrations, either as direct
670 input of DFe or indirectly through Fe-rich sediment carried by the Tagus River and their subsequent
671 dissolution. The Tagus estuary is the largest in the western European coast and very industrialized
672 (Canário et al., 2003; de Barros, 1986; Figueres et al., 1985; Gaudencio et al., 1991; Mil-Homens et
673 al., 2009), that extends through an area of 320 km^2 and is characterized by a large water flow of 15.5
674 10^9 m^3 y^{-1} (Fiuza, 1984). Many types of industry (e.g. heavy metallurgy, ore processing, chemical
675 industry) release metals including Fe, which therefore result in high levels recorded in surface
676 sediments, suspended particulate matter, water and organisms in the lower estuary (Santos-
677 Echeandia et al., 2010).
678

679 **4.3.2 High latitude meteoric water and sea-ice processes**
680 Potential sources of Fe at stations 53, 61 and 78 include meteoric water (MW, referring to
681 precipitation, runoff and continental glacial melt), sea-ice melt (SIM), seawater interaction with shallow
682 sediments and advection of water transported from the Arctic sourced by the Fe-rich TransPolar Drift
683 (TPD, Klunder et al. (2012); see supplementary material Fig. S4 and Table S2). The vertical profiles of
684 both potential temperature and salinity in the Greenland and Newfoundland Margins (station 53, 61
685 and 78, Fig. 4 D, E, and F) highlighted the presence of this freshwater lens likely originating from the
686 Arctic Ocean. They were present in the upper 60 m (station 53) and and 40 m (stations 61 and 78)
687 depth. The most plausible source of this freshwater lens would be meteoric water and sea-ice melting.
688 Deeper in the water column, net brine release (defined as a negative value of sea-ice melting) were
689 observed at stations 53 (below 40 m depth, Fig. 4D) 61 (in the whole water column, Fig. 4E) and 78

690   (below 30 m depth, Fig. 4F). The release of brines could originate from two different processes: the

691   sea-ice formation or the early melting of multiyear sea ice due to gravitational drainage and

692   subsequent brine release (Petrich and Eicken, 2010; Wadhams, 2000). Indeed, during the winter

693   preceding the GEOVIDE voyage, multiyear sea ice extended 200 km off the Greenland stations

694   (http://nsidc.org/arcticseaicenews/). In the following sections, we discuss the potential for meteoric

695   water supply, sea-ice formation and sea-ice melting to affect DFe distribution.

696

697   *4.3.2.1 The Greenland shelf*

698   Considering the sampling period at stations 53 (16 June 2014) and 61 (19 June 2014), sea-ice

699   formation is unlikely to happen as this period coincides with summer melting in both the Central Arctic

700   and East Greenland (Markus et al., 2009). However, it is possible that the brines observed in our study

701   could originates from sea-ice formation which occurred during the previous winter(s) at 66°N (and/or

702   higher latitudes). The brine signalat station 61 between 40 and 140 m was associated with a depletion

703   in both DFe and PFe, which may be attributed to sea ice formation processes. Indeed, as soon as sea

704   ice forms, sea salts are efficiently flushed out of the ice while PFe is trapped within the crystal matrix

705   and DFe accumulates, leading to an enrichment factor of these two Fe fractions compared to

706   underlying seawater (Janssens et al., 2016). Conversely, the strongest brine signal observed at

707   station 53 (between 50 and 160 m) showed slight enrichments in both DFe and PFe, which may be

708   attributed to sea ice melting and the associated release into the underlying water column.

709   Surface waters at stations 53 and 61 were characterized by high MW fractions together with

710   enrichments in PFe at station 53 and in both DFe and PFe at station 61 (Fig. 4D and E). These results

711   are in line with previous observations, which highlighted strong inputs of DFe from a meteoric water

712   melting source in Antarctica (Annett et al., 2015). At station 61, the relative depletion of DFe at 30 m

713   compared to 50 m may be due to phytoplankton uptake, as indicated by the high TChl-*a*

714   concentrations (up to 6.6 mg m^{-3}, Fig. 4D). Hence, it seemed that meteoric water inputs from the

715   Greenland Margin likely fertilized surface waters with DFe, enabling the phytoplankton bloom to

716   subsist.

717

718   *4.3.2.2 The Newfoundland shelf*

719   Newfoundland shelf waters (station 78) were characterized by high MW fractions (up to 7%),

720   decreasing from surface to 200 m depth (~2%). These waters were associated with a net sea-ice

721 melting signal from the near surface to ~10 m depth followed by a brine release signal down to 200 m
722 depth with the maximum contribution measured at ~30 m depth. Within the surface waters (above 20
723 m depth), no elevation in DFe, DAl nor PFe was noticed despite the low measured TChl-*a*
724 concentrations (TChl-*a* ~ 0.20 mg m^{-3}). This suggests that none of these inputs (sea-ice melting and
725 meteoric water) were able to deliver DFe or that these inputs were minor compared to sediment inputs
726 from the Newfoundland Margin. Surprisingly, the highest TChl-*a* biomass (TChl-*a* > 9 mg m^{-3}) from the
727 whole section was measured at 30 m depth corresponding to the strongest brine release signal. This
728 either suggests that the brine likely contained important amounts of Fe (dissolved and/or particulate
729 Fe) that were readily available for phytoplankton and consumed at the sampling period by potentially
730 sea-ice algae themselves (Riebesell et al., 1991) or that another nutrient was triggering the
731 phytoplankton bloom.
732
733 **4.3.3 Atmospheric deposition**
734 On a regional scale, the North Atlantic basin receives the largest amount of atmospheric inputs due to
735 its proximity to the Saharan Desert (Jickells et al., 2005), yet even in this region of high atmospheric
736 deposition, inputs are not evenly distributed. Indeed, aerosol Fe loading measured during GEOVIDE
737 (Shelley et al., 2017) were much lower (up to four orders of magnitude) than those measured during
738 studies from lower latitudes in the North Atlantic (e.g. Baker et al., 2013; Buck et al., 2010; and for
739 GA03, Shelley et al., 2015), but atmospheric inputs could still be an important source of Fe to surface
740 waters in areas far from land.
741 In an attempt to estimate whether there was enough atmospheric input to sustain the SML DFe
742 concentrations, we calculated Turnover Times relative to Atmospheric Deposition (TTADs, Guieu et
743 al., 2014). To do so, we made the following assumptions: 1) the aerosol concentrations are a snapshot
744 in time but are representative of the study region, 2) the aerosol solubility estimates based on two
745 sequential leaches are an upper limit of the aerosol Fe in seawater and 3) the water column stratified
746 just before the deposition of atmospheric inputs, so MLD DFe will reflect inputs from above. Thus, the
747 TTADs were defined as the integrated DFe concentrations in the SML for each station divided by the
748 contribution of soluble Fe contained in aerosols averaged per basin to the water volume of the SML.
749 Although, TTADs were lower in the West European and Iceland Basins with an average of ~ 9 ± 3
750 months compared to other basins (7 ± 2 years and 5 ± 2 years for the Irminger and Labrador Seas,
751 respectively) (Fig. 6) they were about three times higher than those reported for areas impacted by

752 Saharan dust inputs (~ 3 months, Guieu et al., 2014). Therefore, the high TTADs measured in the
753 Irminger and Labrador Seas and ranging from 2 to 15 years provided further evidence that
754 atmospheric deposition were unlikely to supply Fe in sufficient quantity to be the main source of DFe
755 (see Sections 4.2.1 and 4.3.2) while in the West European and Iceland Basins they played an
756 additional source, perhaps the main source of Fe especially at station 36 which displayed TTAD of 3
757 months.
758
759 **4.3.4 Sediment input**
760 *4.3.4.1 Margins:*
761 DFe concentration profiles from all coastal stations (stations 2, 4, 53, 56, 61 and 78) are reported in
762 Figure 4. To avoid surface processes, only depths below 100 m depth will be considered in the
763 following discussion. DFe and PFe followed a similar pattern at stations 2, 53, 56, and 78 with
764 increasing concentrations towards the sediment, suggesting that either the sources of Fe supplied
765 both Fe fractions (dissolved and particulate) or that PFe dissolution from sediments supplied DFe.
766 Among the different margins, the Newfoundland Margin exhibited the highest deep-water DFe and
767 PFe concentrations. Conversely, stations 4 and 61 exhibited a decrease in DFe concentrations in the
768 samples closest to the seafloor whereas PFe increased. DFe:PFe ratios ranged from 0.01 (station 2,
769 bottom sample) to 0.27 (station 4, ~ 400 m depth) mol:mol with an average value of 0.11 ± 0.07
770 mol:mol (n = 23, Table 3). This could be explained by the different nature of the sediments and/or
771 different sediment conditions (e.g. redox, organic content). Based on particulate and dissolved Fe and
772 dissolved Al data (Gourain et al., 2019; Menzel Barraqueta et al., 2018, Table 3), three main different
773 types of margins were reported (Gourain et al., 2019) with the highest lithogenic contribution observed
774 at the Iberian Margin (stations 2 and 4) and the highest biogenic contribution at the Newfoundland
775 Margin (station 78). These observations are consistent with higher TChl-*a* concentrations measured at
776 the Newfoundland Margin and to a lesser extent at the Greenland Margin and the predominance of
777 diatoms relative to other functional phytoplankton classes at both margins (Tonnard et al., in prep.). To
778 sum up, the more biogenic sediments (Newfoundland Margin) were able to mobilise more Fe in the
779 dissolved phase than the more lithogenic sediments (Iberian Margin), in agreement with Boyd et al.
780 (2010) who reported greater remineralization of PFe from biogenic PFe than from lithogenic PFe
781 based on field experiment and modelling simulations.
782

26

4.3.4.2 Nepheloid layers:

Samples associated with high levels of particles (transmissometer < 99%) and below 500 m depth displayed a huge variability in DFe concentrations. From the entire dataset, 63 samples (~13% of the entire dataset) followed this criterion with 14 samples from the West European Basin (station 1), 4 samples from the Iceland Basin (stations 29, 32, 36 and 38), 43 samples from the Irminger Sea (stations 40, 42, 44, 49 and 60) and 2 samples from the Labrador Sea (station 69). To determine which parameter was susceptible to explain the variation in DFe concentrations in these nepheloid layers, a Principal Component Analysis (PCA) on these samples. The input variables of the PCA were particulate Fe, Al, and particulate manganese (PMn) (Gourain et al., 2019), DAl (Menzel Barraqueta et al., 2018) and Apparent Oxygen Utilization (AOU) and were all correlated to DFe concentrations explaining all together 93% of the subset variance (see supplementary material Fig. S6). The first dimension of the PCA was represented by PAl, PFe and PMn concentrations and explained 59.5% of the variance, while the second dimension was represented by the DAl and the AOU parameters, explaining 33.2% of the variance. The two sets of variables were nearly at right angle from each other, indicating no correlation between them.

The variations in DFe concentrations measured in bottom samples from stations 32, 36 (Iceland Basin), 42 and 44 (Irminger Sea) and 69 (Labrador Sea) were mainly explained by the first dimension of the PCA (see supplementary material Fig. S6). Therefore, samples characterized by the lowest DFe concentrations (stations 32 and 69) were driven by particulate Al and Mn concentrations and resulted in an enrichment of Fe in the particulate phase. These results are in agreement with previous studies showing that the presence of Mn within particles can induce the formation of Fe-Mn oxides, contributing to the removal of Fe and Mn from the dissolved phase (Kan et al., 2012; Teng et al., 2001).

Low DFe concentrations (bottom samples from stations 42 and 1) were linked to DAl inputs and associated with lower AOU values. The release of Al has previously been observed from Fe and Mn oxide coatings on resuspended sediments under mildly reducing conditions (Van Beusekom, 1988). Conversely, higher DFe concentrations were observed for stations 44 and 49 and to a lesser extent station 60 coinciding with low DAl inputs and higher oxygen levels. This observation challenges the traditional view of Fe oxidation with oxygen, either abiotically or microbially induced. Indeed, remineralisation can decrease sediment oxygen concentrations, promoting reductive dissolution of PFe oxyhydroxides to DFe that can then diffuse across the sediment water interface as DFe(II)

814   colloids (Homoky et al., 2011). Such processes will inevitably lead to rapid Fe removal through

815   precipitation of nanoparticulate or colloidal Fe (oxyhydr)oxides, followed by aggregation or scavenging

816   by larger particles (Boyd and Ellwood, 2010; Lohan and Bruland, 2008) unless complexion with Fe-

817   binding organic ligands occurs (Batchelli et al., 2010; Gerringa et al., 2008). There exist, however,

818   another process that is favoured in oxic benthic boundary layers (BBL) with low organic matter

819   degradation and/or low Fe oxides, which implies the dissolution of particles after resuspension,

820   namely the non-reductive dissolution of sediment (Homoky et al., 2013; Radic et al., 2011). In addition,

821   these higher oxygenated samples were located within DSOW, which mainly originate (75% of the

822   overflow) from the Nordic Seas and the Arctic Ocean (Tanhua et al., 2005), in which the ultimate

823   source of Fe was reported by Klunder et al. (2012) to come from Eurasian river waters. The major

824   Arctic rivers were highlighted by Slagter et al. (2017) to be a source of Fe-binding organic ligands that

825   are then further transported via the TPD across the Denmark Strait. Hence, the enhanced DFe

826   concentrations measured within DSOW might result from Fe-binding organic ligand complexation that

827   were transported to the deep ocean as DSOW formed rather than the non-reductive dissolution of

828   sediment.

829

830   **4.4 How does biological activity modify DFe distribution?**

831   Overall, almost all the stations from the GEOVIDE voyage displayed DFe minima in surface water

832   associated with some maxima of TChl-*a* (see supplementary material Fig. S1). In the following

833   section, we specifically address the question of whether DFe concentrations potentially limit

834   phytoplankton growth. Note that macronutrients and DFe limitations relative to phytoplankton

835   functional classes are dealt with Tonnard et al. (in prep.).

836   A key determinant for assessing the significance of a DFe source is the magnitude of the

837   DFe:macronutrient ratio supplied, since this term determines to which extent DFe will be utilised. The

838   DFe:NO_3^- ratios in surface waters varied from 0.02 (station 36) to 38.6 (station 61) mmol:mol with an

839   average of 5 ± 10 mmol:mol (see supplementary material Fig. S7). Values were typically equal or

840   lower than 0.28 mmol mol^{-1} in all basins except at the margins and at stations 11, 13, 68, 69 and 77.

841   The low nitrate concentrations observed at the eastern and western Greenland and Newfoundland

842   Margins reflected a strong phytoplankton bloom which had reduced the concentrations as highlighted

843   by the elevated integrated TChl-*a* concentrations ranging from 129.6 (station 78) to 398.3 (station 61)

844   mg m^{-2}. At the Iberian Margin, they likely reflected the influence of the N-limited Tagus River (stations

1, 2 and 4) with its low TChl-*a* integrated concentrations that ranged from 31.2 (station 1) to 46.4 (station 4) mg m^{-2}. The high DFe:NO$_3^-$ ratios determined at those stations, which varied from 13.4 (station 78) to 38.6 (station 61) mmol:mol, suggested that waters from these areas, despite having the lowest NO$_3^-$ concentrations, were relatively enriched in DFe compared to waters from the Iceland Basin and the Irminger Sea.

In our study, DFe:NO$_3^-$ ratios displayed a gradient from the West European Basin to Greenland (supplementary material S7 and S8). This trend only reverses when the influence of Greenland was encountered, as also observed by Painter et al. (2014). The remineralisation of organic matter is a major source of macro and micronutrients in subsurface waters (from 50 to 250 m depth). Remineralisation is associated with the consumption of oxygen and therefore, Apparent Oxygen Utilization (AOU) can provide a quantitative estimate of the amount of material that has been remineralised. While no relationship was observed below 50 m depth for NO$_3^-$ or DFe and AOU considering all the stations, a significant correlation was found in the Subpolar gyre when removing the influence of margins (stations 29-49, 56, 60, 63-77) (AOU = 3.65 NO$_3^-$ – 21.85, R^2=0.70, n=50, p-value < 0.001). This correlation indicates that remineralisation of Particulate Organic Nitrogen (PON) greatly translates into Dissolved Inorganic Nitrogen (DIN) and that NO$_3^-$ can be used as a good tracer for remineralisation in the studied area. Within these Subpolar gyre waters, there was a significant correlation between DFe and AOU (AOU = 23.92 DFe + 10.45, R^2=0.37, n=58, p-value < 0.001). The open-ocean stations from the subpolar gyre also exhibited a good linear correlation between DFe and NO$_3^-$ DFe = 0.08 NO3- - 0.48, R^2=0.45, n=50, p-value < 0.05).(see supplementary material Fig. S8). The negative intercept of the regression line reflects possible excess of preformed NO$_3^-$ compared to DFe in these water masses. These significant correlations allow us to use the Fe* tracer to assess where DFe concentrations potentially limit phytoplankton growth by subtracting the contribution of organic matter remineralisation from the dissolved Fe pool, as defined by Rijkenberg et al. (2014) and Parekh et al. (2005) for PO$_4^{3-}$, and modified here for NO$_3^-$ as follows:

(eq.

where R$_{Fe:N}$ refers to the average biological uptake ratio Fe over nitrogen, and [NO$_3^-$] refers to nitrate concentrations in seawater. Although, we imposed a fixed biological R$_{Fe:N}$ of 0.05 mmol mol^{-1}, it is important to note that the biological uptake ratio of DFe:NO$_3^-$ is not likely to be constant. Indeed, this ratio has been found to range from 0.05 to 0.9 mmol mol^{-1} depending on species (Ho et al., 2003; Sunda and Huntsman, 1995; Twining et al., 2004). The ratio we choose is thus less drastic to assess

29

876   potential Fe limitation and more representative of the average biological uptake of DFe over NO_3^-

877   calculated for this study (i.e. $R_{Fe:N}$ = 0.08 ± 0.01 mmol mol^{-1}, for Subpolar waters). Negative values of

878   Fe* indicate the removal of DFe that is faster than the input through remineralisation or external

879   sources and positive values suggest input of DFe from external sources (Fig. 7). Consequently, figure

880   7 shows that phytoplankton communities with very high Fe requirements relative to NO_3^- ($R_{Fe:N}$ = 0.9

881   mmol mol^{-1}) will only be able to grow above continental shelves where there is a high supply of DFe as

882   previously reported by Nielsdóttir et al. (2009) and Painter et al. (2014). All these results are

883   corroborating the importance of the Tagus River (Iberian Margin, see section 4.2.1), glacial inputs in

884   the Greenland and Newfoundland Margins (see section 4.2.2) and to a lesser extent atmospheric

885   inputs (see section 4.2.3) in supplying Fe with Fe:N ratios higher than the average biological

886   uptake/demand ratio. Figure 7 (see also supplementary material S7, S9, S10 and S11) exhibits Fe:N

887   ratios lower than 0.05 mmol mol^{-1}, suggesting that Fe could also limit the low–Fe requirement

888   phytoplankton class ($R_{Fe:N}$ = 0.05 mmol mol^{-1}) within the Iceland Basin, the Irminger, and the Labrador

889   Seas. The Fe deficiency observed in surface waters (> 50 m depth) from the Irminger and the

890   Labrador Seas might be explained by low atmospheric deposition to IcSPMW and LSW (Shelley et al.,

891   2017). Low atmospheric Fe supply and sub-optimal Fe:N ratios in winter overturned deep water could

892   favour the formation of the High-Nutrient, Low-Chlorophyll (HNLC) conditions. The West European

893   Basin, despite exhibiting some of the highest DFe:NO_3^- ratios within surface waters, displayed one of

894   the strongest Fe-depletions from 50 m depth down to the bottom (see supplementary material Fig. S9

895   and S10), suggesting that the main source of Fe was coming from dust deposition and/or riverine

896   inputs.

897   Similarly as for the West European Basin, the pattern displayed in the surface map of DFe:NO_3^- ratios

898   (supplementary material S9) extended to about 50 m depth, after which the trend reversed (Fig. 7 and

899   supplementary material Fig. S7). Below 50 m depth, the Fe* tracer (Fig. 7) was positive in the Irminger

900   Sea and overall negative in the other basins. In the Irminger Sea positive Fe* values were likely the

901   result of the winter entrainment of Fe-rich LSW (see section 4.2.1) coinciding with high remineralised

902   carbon fluxes in this area (station 44; Lemaître et al., 2017) (see section 4.2.2). The largest drawdown

903   in DFe:NO_3^- ratios was observed between stations 34 and 38 and was likely due to the intrusion of

904   IcSPMW, this water mass exhibiting low DFe and high in NO_3^- (from 7 to 8 µmol L^{-1}) concentrations.

905   Similarly, SAIW exhibited high NO_3^- concentrations. Both the IcSPMW and the SAIW sourced from the

906   NAC. The NAC as it flows along the coast of North America receives atmospheric depositions from

907 anthropogenic sources (Shelley et al., 2017; 2015) which deliver high N relative to Fe (Jickells and
908 Moore, 2015) and might be responsible for the observed ranges.
909
910 **5 Conclusion**
911 The DFe concentrations measured during this study were in good agreement with previous studies
912 that spanned the West European Basin. However, within the Irminger Basin the DFe concentrations
913 measured during this study were up to 3 times higher than those measured by Rijkenberg et al. (2014)
914 in deep waters (> 1000 m depth). This is likely explained by the different water masses encountered
915 (i.e. the Polar Intermediate Water, ~ 2800 m depth) and by a stronger signal of the Iceland Scotland
916 Overflow Water (ISOW) from 1200 to 2300 m depth. This corresponded to the most striking feature of
917 the whole section with DFe concentrations reaching up to 2.5 nmol L^{-1} within ISOW, Denmark Strait
918 Overflow Water (DSOW) and Labrador Sea Water (LSW), three water masses that are part of the
919 Deep Western Boundary Current and was likely the result of a lateral advection of particles in the
920 Irminger Sea. However, as these water masses reached the Labrador Sea, lower DFe levels were
921 measured. These differences could be explained by different processes occurring within the benthic
922 nepheloid layers, where DFe was sometimes trapped onto particles due to Mn-sediment within the
923 Labrador Sea (Gourain et al., 2019) and sometimes released from the sediment potentially as a result
924 of interactions with dissolved organic matter. Such Fe-binding organic ligands could have also been
925 produced locally due to the intense remineralisation rate reported by Lemaître et al. (2017) of biogenic
926 particles (Boyd et al., 2010; Gourain et al., 2019). The LSW exhibited increasing DFe concentrations
927 along its flow path, likely resulting from sediment inputs at the Newfoundland Margin. Although DFe
928 inputs through hydrothermal activity were expected at the slow spreading Reykjanes Ridge (Baker and
929 German, 2004; German et al., 1994), our data did not provide evidence of this specific source as
930 previously suggested by Achterberg et al. (2018) at ~60°N.
931 In surface waters several sources of DFe were highlighted especially close to land, with riverine inputs
932 from the Tagus River at the Iberian margin (Menzel Barraqueta et al., 2018) and meteoric inputs
933 (including coastal runoff and glacial meltwater) at the Newfoundland and the Greenland margins
934 (Benetti et al., 2016). Substantial sediment input was observed at all margins but with varying
935 intensity. The highest DFe sediment input was located at the Newfoundland margin, while the lowest
936 was observed at the eastern Greenland margin. These differences could be explained by the different
937 nature of particles with the most lithogenic located at the Iberian margin and the most biogenic, at the

31

938   Newfoundland margin (Gourain et al., 2019). Although previous studies (e.g. Jickells et al., 2005;
939   Shelley et al., 2015) reported that atmospheric inputs substantially fertilized surface waters from the
940   West European Basin, in our study, only stations located in the West European and Iceland Basins
941   exhibited enhanced SML DFe inventories with lower TTADs. However, these TTADs were about three
942   times higher than those reported for Saharan dust inputs and thus atmospheric deposition appeared to
943   be a minor source of Fe during the sampling period. Finally, there was evidence of convective inputs
944   of the LSW to surface seawater caused by long tip jet events (Piron et al., 2016) that deepened the
945   winter mixed layer down to ~ 1200 m depth (Zunino et al., 2017), in which Fe was in excess of nitrate
946   and therefore, Fe was not limiting.

947

964

965   All dissolved iron (DFe) data are available in the supplementary material S1.

966

References

Achterberg, E. P., Steigenberger, S., Marsay, C. M., LeMoigne, F. A., Painter, S. C., Baker, A. R., Connelly, D. P., Moore, C. M., Tagliabue, A., and Tanhua, T.: Iron Biogeochemistry in the High Latitude North Atlantic Ocean, Scientific reports, 8, 1-15, 10.1038/s41598-018-19472-1, 2018.

Aminot, A., and Kerouel, R.: Dosage automatique des nutriments dans les eaux marines, Quae ed., 2007.

Annett, A. L., Skiba, M., Henley, S. F., Venables, H. J., Meredith, M. P., Statham, P. J., and Ganeshram, R. S.: Comparative roles of upwelling and glacial iron sources in Ryder Bay, coastal western Antarctic Peninsula, Marine Chemistry, 176, 21-33, 10.1016/j.marchem.2015.06.017, 2015.

Armi, L., Hebert, D., Oakey, N., Price, J., Richardson, P. L., Rossby, T. and Ruddick, B.: The history and decay of a Mediterranean salt lens, Nature, 333(6174), 649–651, doi:10.1038/333649a0, 1988.

Bacon, S., Gould, W. J., and Jia, Y.: Open-ocean convection in the Irminger Sea, Geophysical Research Letters, 30, 1246, doi:10.1029/2002GL016271, 2003.

Baker, A. R., Adams, C., Bell, T. G., Jickells, T. D., and Ganzeveld, L.: Estimation of atmospheric nutrient inputs to the Atlantic Ocean from 50°N to 50°S based on large-scale field sampling: Iron and other dust-associated elements, Global Biogeochemical Cycles, 27, 755-767, 10.1002/gbc.20062, 2013.

Baker, A. T., and German, C. R.: On the Global Distribution of Hydrothermal vent Fields, . In Mid-Ocean Ridges: Hydrothermal Interactions Between the Lithosphere and Oceans, Geophysical Monograph Series 148, C.R. German, J. Lin, and L.M. Parson (eds.), 245–266 (2004)

Barton, A. D., Greene, C. H., Monger, B. C., and Pershing, A. J.: The Continuous Plankton Recorder survey and the North Atlantic Oscillation: Interannual- to Multidecadal-scale patterns of phytoplankton variability in the North Atlantic Ocean, Progress in Oceanography, 58, 337-358, 10.1016/j.pocean.2003.08.012, 2003.

Batchelli, S., Muller, F. L. L., Chang, K. C., and Lee, C. L.: Evidence for Strong but Dynamic Iron-Humic Colloidal Associations in Humic-Rich Coastal Waters., Environmental Science & Technology, 44, 8485-8490, https://doi.org/10.1021/es101081c, 2010.

997 Benetti, M., Reverdin, G., Pierre, C., Khatiwala, S., Tournadre, B., Olafsdottir, S., and Naamar, A.:
998   Variability of sea ice melt and meteoric water input in the surface Labrador Current off
999   Newfoundland, Journal of Geophysical Research Oceans, 121, 2841-2855,
1000   doi:10.1002/2015JC011302., 2016.

1001 Benetti, M., Reverdin, G., Lique, C., Yashayaev, I., Holliday, N. P., Tynan, E., Torres-Valdes, S.,
1002   Lherminier, P., Tréguer, P., and Sarthou, G.: Composition of freshwater in the spring of 2014 on
1003   the southern Labrador shelf and slope, Journal of Geophysical Research: Oceans, 122, 1102-
1004   1121, 10.1002/2016jc012244, 2017.

1005 Bergquist, B. A. and Boyle, E. A.: Dissolved iron in the tropical and subtropical Atlantic Ocean, Global
1006   Biogeochemical Cycles, 20(1), doi:10.1029/2005GB002505, 2006.

1007 Bersch, M., Yashayaev, I., and Koltermann, K. P.: Recent changes of the thermohaline circulation in
1008   the subpolar North Atlantic, Ocean Dynamics, 57, 223-235, 10.1007/s10236-007-0104-7, 2007.

1009 Bhatia, M. P., Kujawinski, E. B., Das, S. B., Breier, C. F., Henderson, P. B., and Charette, M. A.:
1010   Greenland meltwater as a significant and potentially bioavailable source of iron to the ocean,
1011   Nature Geoscience, 2013, 274-278, 10.1038/ngeo1746, 2013.

1012 Bonnet, S., and Guieu, C.: Dissolution of atmospheric iron in seawater, Geophysical Research Letters,
1013   31, 10.1029/2003gl018423, 2004.

1014 Bonnet, S., and Guieu, C.: Atmospheric forcing on the annual iron cycle in the western Mediterranean
1015   Sea: A 1-year survey, Journal of Geophysical Research, 111, 10.1029/2005jc003213, 2006.

1016 Boyd, P. W., Watson, A. J., Law, C. S., Abraham, E. R., Trull, T., Murdoch, R., Bakker, D. C. E.,
1017   Bowie, A. R., Buesseler, K. O., Chang, H., Charette, M., Croot, P., Downing, K., Frew, R., Gall, M.,
1018   Hadfield, M., Hall, J., Harvey, M., Jameson, G., LaRoche, J., Liddicoat, M., Ling, R., Maldonado, M.
1019   T., McKay, R. M., Nodder, S., Pickmere, S., Pridmore, R., Rintoul, S., Safi, K., Sutton, P., Strzepek,
1020   R., Tanneberger, K., Turner, S., Waite, A., and Zeldis, J.: A mesoscale phytoplankton bloom in the
1021   polar Southern Ocean stimulated by iron fertilization, Nature, 407, 695-702, 10.1038/35037500,
1022   2000.

1023 Boyd, P. W., and Ellwood, M. J.: The biogeochemical cycle of iron in the ocean, Nature Geoscience,
1024   3, 675-682, 10.1038/ngeo964, 2010.

1025 Boyd, P. W., Ibisanmi, E., Sander, S. G., Hunter, K. A., and Jackson, G. A.: Remineralization of upper
1026   ocean particles: Implications for iron biogeochemistry, Limnology and Oceanography, 55, 1271-
1027   1288, 10.4319/lo.2010.55.3.1271, 2010.

1028   Buck, C. S., Landing, W. M., Resing, J. A., and Measures, C. I.: The solubility and deposition of
1029   aerosol Fe and other trace elements in the North Atlantic Ocean: Observations from the A16N
1030   CLIVAR/CO2 repeat hydrography section, Marine Chemistry, 120, 57-70,
1031   10.1016/j.marchem.2008.08.003, 2010.

1032   Canário, J., Vale, C., Caetano, M., and Madureira, M. J.: Mercury in contaminated sediments and pore
1033   waters enriched in sulphate (Tagus Estuary, Portugal), Environmental Pollution, 126, 425-433,
1034   10.1016/S0269-7491(03)00234-3, 2003.

1035   Charette, M. A., Morris, P. J., Henderson, P. B., and Moore, W. S.: Radium isotope distributions during
1036   the US GEOTRACES North Atlantic cruises, Marine Chemistry, 177, 184-195,
1037   10.1016/j.marchem.2015.01.001, 2015.

1038   Chen, Y. J.: Influence of the Iceland mantle plume on crustal accretion at the inflated Reykjanes
1039   Ridge: Magma lens and low hydrothermal activity, Journal of Geophysical Research, 108, 2524,
1040   https://doi-org.inee.bib.cnrs.fr/10.1029/2001JB000816, 2003.

1041   Chester, R., Murphy, K. J. T., Lin, F. J., Berry, A. S., Bradshaw, G. A., and Corcoran, P. A.: Factors
1042   controlling the solubilities of trace-metals from nonremote aerosols deposited to the sea-surface by
1043   the dry deposition mode, Marine Chemistry, 42, 107-126, 10.1016/0304-4203(93)90241-f, 1993.

1044   Conway, T. M., and John, S. G.: Quantification of dissolved iron sources to the North Atlantic Ocean,
1045   Nature, 511, 212-215, 10.1038/nature13482, 2014.

1046   Cooper, L. W., Whitledge, T. E., Grebmeier, J. M., and Weingartner, T.: The nutrient, salinity, and
1047   stable oxygen isotope composition of Bering and Chukchi Seas waters in and near the Bering
1048   Strait, Journal of Geophysical Research, 102, 12,563-512,573, 1997.

1049   Cooper, L. W., McClelland, J. W., Holmes, R. M., Raymond, P. A., Gibson, J. J., Guay, C. K., and
1050   Peterson, B. J.: Flow-weighted values of runoff tracers (δ18O, DOC, Ba, alkalinity) from the six
1051   largest Arctic rivers, Geophysical Research Letters, 35, 1-5, 10.1029/2008GL035007, 2008.

1052

1053   Crane, K., Johnson, L., Appelgate, B., Nishimura, C., Buck, R., Jones, C., Vogt, P., and Kos'yan, R.
1054   Volcanic and Seismic Swarm Events on the Reykjanes Ridge and Their Similarities to Events on
1055   Iceland: Results of a Rapid Response Mission. Marine Geophysical Researches (1997) 19: 319.
1056   https://doi.org/10.1023/A:1004298425881

1057   Croot, P. L., Streu, P. and Baker, A. R.: Short residence time for iron in surface seawater impacted by
1058   atmospheric dry deposition from Saharan dust events, Geophys. Res. Lett., 31(L23S08), doi:
1059   10.1029/2004GL020153, 2004.

1060   Cutter, G., Casciotti, K., Croot, P., Geibert, W., Heimburger, L. E., Lohan, M., Planquette, H., and van
1061   de Flierdt, T.: Sampling and the Sample-handling Protocols for GEOTRACES Cruises, 2017.

1062   Daniault, N., Mercier, H., Lherminier, P., Sarafanov, A., Falina, A., Zunino, P., Pérez, F. F., Ríos, A. F.,
1063   Ferron, B., Huck, T., Thierry, V., and Gladyshev, S.: The northern North Atlantic Ocean mean
1064   circulation in the early 21st century, Progress in Oceanography, 146, 142-158,
1065   10.1016/j.pocean.2016.06.007, 2016.

1066   de Baar, H. J. W. and de Jong, J. T. M.: Distributions, Sources and Sinks of Iron in Seawater, in
1067   Biogeochemistry of Fe in Seawater, vol. Chapter 5, edited by D. R. Turner and K. A. Hunter, pp.
1068   123–253, SCOR-IUPAC series, J Wiley, Baltimore., 2001.

1069   de Barros, M. C.: A case study of waste inputs in the Tagus estuary, in: The role of the Oceans as a
1070   Waste Disposal Option, edited by: Kullenberg, G., NATO ASI Series; Series C: Mathematical and
1071   Physical Sciences, 172, Springer Netherlands, 307-324, 1986.

1072   de Jong, M. F., van Aken, H. M., Våge, K., and Pickart, R. S.: Convective mixing in the central
1073   Irminger Sea: 2002–2010, Deep Sea Research Part I: Oceanographic Research Papers, 63, 36-
1074   51, 10.1016/j.dsr.2012.01.003, 2012.

1075   Dehairs, F., Shopova, D., Ober, S., Veth, C., and Goeyens, L.: Particulate barium stocks and oxygen
1076   consumption in the Southern Ocean mesopelagic water column during spring and early summer:
1077   Relationship with export production, Deep Sea Research II, 44, 497-516, 10.1016/S0967-
1078   0645(96)00072-0, 1997.

1079   Deng, F., Henderson, G. M., Castrillejo, M., and Perez, F. F.: Evolution of ^{231}Pa and ^{230}Th in overflow
1080   waters of the North Atlantic, Biogeosciences, 15, 7299–7313, https://doi.org/10.5194/bg-15-7299-
1081   2018, 2018.

1082   Fagel, N., Robert, C., and Hilaire-Marcel, C.: Clay mineral signature of the NW Atlantic Boundary
1083   Undercurrent, Marine Geology, 130, 19-28, https://doi.org/10.1016/0025-3227(95)00134-4, 1996.

1084   Fagel, N., Robert, C., Preda, M., and Thorez, J.: Smectite composition as a tracer of deep circulation:
1085   the case of the Northern North Atlantic, Marine Geology, 172, 309-330,
1086   https://doi.org/10.1016/S0025-3227(00)00123-7, 2001.

1087 Ferron, B., Kokoszka, F., Mercier, H., Lherminier, P., Huck, T., Rios, A., and Thierry, V.: Variability of
1088   the Turbulent Kinetic Energy Dissipation along the A25 Greenland–Portugal Transect Repeated
1089   from 2002 to 2012, Journal of Physical Oceanography, 46, 1989-2003, 10.1175/jpo-d-15-0186.1,
1090   2016.
1091 Figueres, G., Martin, J. M., Meybeck, M., and Seyler, P.: A comparative study of mercury
1092   contamination in the Tagus estuary (Portugal) and major French estuaries (Gironde, Loire, Rhone),
1093   Estuarine, Coastal and Shelf Science, 20, 183-203, https://doi.org/10.1016/0272-7714(85)90037-X,
1094   1985.
1095 Fiuza, A.: Hidrologia e dinamica das aguas costeiras de Portugal, Ph. D., Universidade de Lisboa,
1096   Lisboa, Portugal, unpublished, 1984.
1097 Follows, M., and Dutkiewicz, S.: Meteorological modulation of the North Atlantic Spring Bloom, Deep
1098   Sea Research Part II: Topical Studies in Oceanography, 49, 321-344,
1099   https://doi.org/10.1016/S0967-0645(01)00105-9, 2001.
1100 García-Ibáñez, M. I., Pardo, P. C., Carracedo, L. I., Mercier, H., Lherminier, P., Ríos, A. F., and Pérez,
1101   F. F.: Structure, transports and transformations of the water masses in the Atlantic Subpolar Gyre,
1102   Progress in Oceanography, 135, 18-36, 10.1016/j.pocean.2015.03.009, 2015.
1103 García-Ibáñez, M. I., Pérez, F. F., Lherminier, P., Zunino, P., Mercier, H., and Tréguer, P.: Water
1104   mass distributions and transports for the 2014 GEOVIDE cruise in the North Atlantic,
1105   Biogeosciences, 15, 2075-2090, 10.5194/bg-15-2075-2018, 2018.
1106 Gaudencio, M. J., Guerra, M. T., and Glemarec, M.: Recherches biosedimentaires sur la zone
1107   maritime de l'estuaire du Tage, Portugal: donnees sedimentaires preliminaires. , in: Estuaries and
1108   Coasts: Spatial and Temporal Intercomparisons, edited by: Elliot, M., and Ducrotoy, J. C., Olsen
1109   and Olsen, Fredensborg, 11-16, 1991.
1110 German, C. R., Briem, J., Chin, C. S., Danielsen, M., Holland, S., James, R. H., Jonsdottir, A.,
1111   Ludford, E., Moser, C., Olafsson, J., Palmer, M. R., and Rudnicki, M. D.: Hydrothermal activity on
1112   the Reykjanes Ridge: the Steinahóll vent-field at 63°06′N, Earth and Planetary Science Letters,
1113   121, 647-654, https://doi.org/10.1016/0012-821X(94)90098-1, 1994.
1114 Gerringa, L. J. A., Blain, S., Laan, P., Sarthou, G., Veldhuis, M. J. W., Brussaard, C. P. D., Viollier, E.,
1115   and Timmermans, K. R.: Fe-binding dissolved organic ligands near the Kerguelen Archipelago in
1116   the Southern Ocean (Indian sector), Deep Sea Research Part II: Topical Studies in Oceanography,
1117   55, 606-621, 10.1016/j.dsr2.2007.12.007, 2008.

1118   Gerringa, L. J. A., Rijkenberg, M. J. A., Schoemann, V., Laan, P. and de Baar, H. J. W.: Organic
1119   complexation of iron in the West Atlantic Ocean, Marine Chemistry, 177, 434–446,
1120   doi:10.1016/j.marchem.2015.04.007, 2015.

1121   Gerringa, L. J. A., Slagter, H. A., Bown, J., van Haren, H., Laan, P., de Baar, H. J. W., and Rijkenberg,
1122   M. J. A.: Dissolved Fe and Fe-binding organic ligands in the Mediterranean Sea – GEOTRACES
1123   G04, Marine Chemistry, 194, 100-113, 10.1016/j.marchem.2017.05.012, 2017.

1124   Gourain, A., Planquette, H., Cheize, M., Lemaitre, N., Menzel Barraqueta, J.-L., Shelley, R.,
1125   Lherminier, P., and Sarthou, G.: Inputs and processes affecting the distribution of particulate iron in
1126   the North Atlantic along the GEOVIDE (GEOTRACES GA01) section, Biogeosciences, 16, 1563–
1127   1582, https://doi.org/10.5194/bg-16-1563-2019, 2019.

1128   Guerzoni, S., Chester, R., Dulac, F., Herut, B., Loye-Pilot, M.-D., Measures, C., Migon, C., Molinaroli,
1129   E., Moulin, C., Rossini, P., Saydam, C., Soudine, A., and Ziveri, P.: The role of atmospheric
1130   deposition in the biogeochemistry of the Mediterranean Sea, Progress in Oceanography, 44, 147-
1131   190, https://doi.org/10.1016/S0079-6611(99)00024-5, 1999.

1132   Guieu, C., Loÿe-Pilot, M. D., Benyahya, L., and Dufour, A.: Spatial variability of atmospheric fluxes of
1133   metals (Al, Fe, Cd, Zn and Pb) and phosphorus over the whole Mediterranean from a one-year
1134   monitoring experiment: Biogeochemical implications, Marine Chemistry, 120, 164-178,
1135   10.1016/j.marchem.2009.02.004, 2010.

1136   Guieu, C., Aumont, O., Paytan, A., Bopp, L., Law, C. S., Mahowald, N., Achterberg, E. P., Marañón,
1137   E., Salihoglu, B., Crise, A., Wagener, T., Herut, B., Desboeufs, K., Kanakidou, M., Olgun, N.,
1138   Peters, F., Pulido-Villena, E., Tovar-Sanchez, A., and Völker, C.: The significance of the episodic
1139   nature of atmospheric deposition to Low Nutrient Low Chlorophyll regions, Global Biogeochemical
1140   Cycles, 28, 1179-1198, 10.1002/2014gb004852, 2014.

1141   Harrison, W. G., Yngve Børsheim, K., Li, W. K. W., Maillet, G. L., Pepin, P., Sakshaug, E., Skogen, M.
1142   D., and Yeats, P. A.: Phytoplankton production and growth regulation in the Subarctic North
1143   Atlantic: A comparative study of the Labrador Sea-Labrador/Newfoundland shelves and
1144   Barents/Norwegian/Greenland seas and shelves, Progress in Oceanography, 114, 26-45,
1145   10.1016/j.pocean.2013.05.003, 2013.

1146   Hatta, M., Measures, C. I., Wu, J., Roshan, S., Fitzsimmons, J. N., Sedwick, P., and Morton, P.: An
1147   overview of dissolved Fe and Mn distributions during the 2010-2011 US GEOTRACES north

1148   Atlantic cruises: GEOTRACES GA03, Deep-Sea Research Part Ii-Topical Studies in
1149   Oceanography, 116, 117-129, 10.1016/j.dsr2.2014.07.005, 2015.

1150 Hawkings, J. R., Wadham, J. L., Tranter, M., Raiswell, R., Benning, L. G., Statham, P. J., Tedstone,
1151   A., Nienow, P., Lee, K., and Telling, J.: Ice sheets as a significant source of highly reactive
1152   nanoparticulate iron to the oceans, Nature communications, 5, 1-8, 10.1038/ncomms4929, 2014.

1153 Henson, S. A., Dunne, J. P., and Sarmiento, J. L.: Decadal variability in North Atlantic phytoplankton
1154   blooms, Journal of Geophysical Research, 114, 10.1029/2008jc005139, 2009.

1155 Ho, T.-Y., Quigg, A., Finkel, Z. V., Milligan, A. J., Wyman, K., Falkowski, P. G., and Morel, F. M. M.:
1156   The elemental composition of some marine phytoplankton, Journal of Phycology, 39, 1145-1159,
1157   https://doi.org/10.1111/j.0022-3646.2003.03-090.x, 2003.

1158 Homoky, W. B., Hembury, D. J., Hepburn, L. E., Mills, R. A., Statham, P. J., Fones, G. R., and Palmer,
1159   M. R.: Iron and manganese diagenesis in deep sea volcanogenic sediments and the origins of pore
1160   water colloids, Geochimica Et Cosmochimica Acta, 75, 5032-5048, 10.1016/j.gca.2011.06.019,
1161   2011.

1162 Homoky, W. B., John, S. G., Conway, T. M., and Mills, R. A.: Distinct iron isotopic signatures and
1163   supply from marine sediment dissolution, Nature Communications, 4, 10.1038/ncomms3143, 2013.

1164 Humphreys, M. P., Griffiths, A. M., Achterberg, E. P., Holliday, N. P., Rérolle, V., Menzel Barraqueta,
1165   J. L., Couldrey, M. P., Oliver, K. I., Hartman, S. E., and Esposito, M.: Multidecadal accumulation of
1166   anthropogenic and remineralized dissolved inorganic carbon along the Extended Ellett Line in the
1167   northeast Atlantic Ocean, Global Biogeochemical Cycles, 30, 293-310, doi:
1168   10.1002/2015GB005246, 2016.

1169 Hunke, E. C., Notz, D., Turner, A. K., and Vancoppenolle, M.: The multiphase physics of sea ice: a
1170   review for model developers, The Cryosphere, 5, 989-1009, 10.5194/tc-5-989-2011, 2011.

1171 Janssens, J., Meiners, K. M., Tison, J.-L., Dieckmann, G., Delille, B., and Lannuzel, D.: Incorporation
1172   of iron and organic matter into young Antarctic sea ice during its initial growth stages, Elementa:
1173   Science of the Anthropocene, 4, 000123, 10.12952/journal.elementa.000123, 2016.

1174 Jickells, T., and Moore, C. M.: The importance of atmospheric deposition for ocean productivity,
1175   Annual Review of Ecology, Evolution, and Systematics, 46, 481-501, 10.1146/annurev-ecolsys-
1176   112414-054118, 2015.

1177 Jickells, T. D., An, Z. C., Andersen, K. K., Baker, A. R., Bergametti, G., Brooks, N., Cao, J. J., Boyd, P.
1178   W., Duce, R. A., Hunter, K. A., Kawahata, H., Kubilay, N., laRoche, J., Liss, P. S., Mahowald, N.,

1179   Prospero, J. M., Ridgwell, A. J., Tegen, I., and Torres, R.: Global iron connections between desert
1180   dust, ocean biogeochemistry, and climate, Science, 308, 67-71, DOI: 10.1126/science.1105959,
1181   2005.

1182   Jones, E. P., Anderson, L. G., and Swift, J. H.: Distribution of Atlantic and Pacific waters in the upper
1183   Arctic Ocean: Implications for circulation, Geophysical Research Letters, 25, 765-768, https://doi-
1184   org.inee.bib.cnrs.fr/10.1029/98GL00464, 1998.

1185   Kan, C. C., Chen, W. H., Wan, M. W., Phatai, P., Wittayakun, J., and Li, K. F.: The preliminary study of
1186   iron and manganese removal from groundwater by NaOCl oxidation and MF filtration, Sustain.
1187   Environ. Res., 22, 25-30, 2012.

1188   Kanzow, T. and Zenk, W.: Structure and transport of the Iceland Scotland Overflow plume along the
1189   Reykjanes Ridge in the Iceland Basin, Deep Sea Research Part I: Oceanographic Research
1190   Papers, 86, 82–93, doi:10.1016/j.dsr.2013.11.003, 2014

1191   Kara, A. B., Rochford, P. A., and Hurlburt, H. E.: An optimal definition for ocean mixed layer depth,
1192   Journal of Geophysical Research, 105, 16,803-816,821, 10.1029/2000JC900072, 2000.

1193   Käse, R. H., Girton, J. B. and Sanford, T. B.: Structure and variability of the Denmark Strait Overflow:
1194   Model and observations, Journal of Geophysical Research: Oceans, 108(C6),
1195   doi:10.1029/2002JC001548, 2003.

1196   Kissel, C., Laj, C., Mulder, T., Wandres, C., and Cremer, M.: The magnetic fraction: A tracer of deep
1197   water circulation in the North Atlantic, Earth and Planetary Science Letters, 288, 444-454,
1198   10.1016/j.epsl.2009.10.005, 2009.

1199   Klunder, M. B., Bauch, D., Laan, P., de Baar, H. J. W., van Heuven, S. M. A. C., and Ober, S.:
1200   Dissolved iron in the Arctic shelf seas and surface waters of the Central Arctic Ocean: impact of
1201   Arctic river water and ice-melt, Journal of Geophysical Research, 117, 1-18, https://doi-
1202   org.inee.bib.cnrs.fr/10.1029/2011JC007133, 2012.

1203   Lackschewitz, K. S., Endler, R., Gehrke, B., Wallrabe-Adams, H.-J., and Thiede, J.: Evidence for
1204   topography- and current-controlled deposition on the reykjanes Ridge between 59°N and 60°N,
1205   Deep-Sea Research I, 43, 1683-1711, https://doi.org/10.1016/S0967-0637(96)00090-8, 1996.

1206   Laes, A., Blain, S., Laan, P., Achterberg, E. P., Sarthou, G., and de Baar, H. J. W.: Deep dissolved
1207   iron profiles in the eastern North Atlantic in relation to water masses, Geophysical Research
1208   Letters, 30, 10.1029/2003gl017902, 2003.

1209 Lagerström, M. E., Field, M. P., Seguret, M., Fischer, L., Hann, S., and Sherrell, R. M.: Automated on-
1210   line flow-injection ICP-MS determination of trace metals (Mn, Fe, Co, Ni, Cu and Zn) in open ocean
1211   seawater: Application to the GEOTRACES program, Marine Chemistry, 155, 71-80,
1212   10.1016/j.marchem.2013.06.001, 2013.
1213 Lambelet, M., van de Flierdt, T., Crocket, K., Rehkamper, M., Katharina, K., Coles, B., Rijkenberg, M.
1214   J. A., Gerringa, L. J. A., de Baar, H. J. W., and Steinfeldt, R.: Neodymium isotopic composition and
1215   concentration in the western North Atlantic Ocean: Results from the GEOTRACES GA02 section,
1216   Geochimica Et Cosmochimica Acta, 177, 1-29, https://doi.org/10.1016/j.gca.2015.12.019, 2016.
1217 Le Roy, E., Sanial, V., Charette, M. A., van Beek, P., Lacan, F., Jacquet, S. H. M., Henderson, P. B.,
1218   Souhaut, M., García-Ibáñez, M. I., Jeandel, C., Pérez, F. F., and Sarthou, G.: The ^{226}Ra–Ba
1219   relationship in the North Atlantic during GEOTRACES-GA01, Biogeosciences, 15, 3027-3048,
1220   10.5194/bg-15-3027-2018, 2018.
1221 Lemaitre, N., Planchon, F., Planquette, H., Dehairs, F., Fonseca-Batista, D., Roukaerts, A., Deman,
1222   F., Tang, Y., Mariez, C., and Sarthou, G.: High variability of particulate organic carbon export along
1223   the North Atlantic GEOTRACES section GA01 as deduced from 234Th fluxes, Biogeosciences, 15,
1224   6417–6437, https://doi.org/10.5194/bg-15-6417-2018, 2018. .
1225 Lemaitre, N., Planquette, H., Planchon, F., Sarthou, G., Jacquet, S., García-Ibáñez, M. I., Gourain, A.,
1226   Cheize, M., Monin, L., André, L., Laha, P., Terryn, H., and Dehairs, F.: Particulate barium tracing of
1227   significant mesopelagic carbon remineralisation in the North Atlantic, Biogeosciences, 15, 2289–
1228   2307, https://doi.org/10.5194/bg-15-2289-2018, 2018.
1229 Lohan, M. C., and Bruland, K. W.: Elevated Fe(II) and Dissolved Fe in Hypoxic Shelf Waters off
1230   Oregon and Washington: An Enhanced Source of Iron to Coastal Upwelling Regimes,
1231   Environmental Science & Technology, 42, 6462-6468, 10.1021/es800144j, 2008.
1232 Longhurst, A. R.: Ecological geography of the Sea, Second Edition ed., Elsevier Academic Press
1233   publications, Burlington, 542 pp., 2007.
1234 Louanchi, F., and Najjar, R. G.: Annual cycles of nutrients and oxygen in the upper layers of the North
1235   Atlantic Ocean, Deep Sea Research Part II: Topical Studies in Oceanography, 48, 2155-2171,
1236   https://doi.org/10.1016/S0967-0645(00)00185-5, 2001.
1237 Markus, T., Stroeve, J. C., and Miller, J.: Recent changes in Arctic sea ice melt onset, freezeup, and
1238   melt season length, Journal of Geophysical Research, 114, 10.1029/2009jc005436, 2009.

1239   Marshall, J., and Schott, F.: Open-ocean convection: observations, theory, and models, Reviews of

1240   Geophysics, 37, 1-64, doi: 10.1029/98RG02739, 1999.

1241   Martin, J.-M., Elbaz-Poulichet, F., Guieu, C., Loÿe-Pilot, M.-D., and Han, G.: River versus atmospheric

1242   input of material to the Mediterranean Sea: an overview, Marine Chemistry, 28, 159-182,

1243   https://doi.org/10.1016/0304-4203(89)90193-X, 1989.

1244   Martin, J. D., and Fitzwater, S. E.: Iron deficiency limits phytoplankton growth in the north-east Pacific

1245   subarctic, Nature, 331, 341-343, 1988.

1246   Martin, J. H., Fitzwater, S. E., and Gordon, R. M.: Iron deficiencies limits phytoplankton growth in

1247   Antarctic waters, Global Biogeochemical Cycles, 4, 5-12, https://doi-

1248   org.inee.bib.cnrs.fr/10.1029/GB004i001p00005, 1990.

1249   Martin, J. H., Coale, K. H., Johnson, K. S., Fitzwater, S. E., Gordon, R. M., Tanner, S. J., Hunter, C.

1250   N., Elrod, V. A., Nowicki, J. L., Coley, T. L., Barber, R. T., Lindley, S., Watson, A. J., Van Scoy, K.,

1251   Law, C. S., Liddicoat, M. I., Ling, R., Stanton, T., Stockel, J., Collins, C., Anderson, A., Bidigare, R.,

1252   Ondrusek, M., Latasa, M., Millero, F. J., Lee, K., Yao, W., Zhang, J. Z., Friederich, G., Sakamoto,

1253   C., Chavez, F., Buck, K., Kolber, Z., Greene, R., Falkowski, P., Chisholm, S. W., Hoge, F., Swift,

1254   R., Yungel, J., Turner, S., Nightingale, P., Hatton, A., Liss, P., and Tindale, N. W.: Testing the Iron

1255   Hypothesis in Ecosystems of the Equatorial Pacific Ocean, Nature, 371, 123-129,

1256   10.1038/371123a0, 1994.

1257   Measures, C. I., Brown, M. T., Selph, K. E., Apprill, A., Zhou, M., Hatta, M., and Hiscock, W. T.: The

1258   influence of shelf processes in delivering dissolved iron to the HNLC waters of the Drake Passage,

1259   Antarctica, Deep Sea Research Part II: Topical Studies in Oceanography, 90, 77-88,

1260   10.1016/j.dsr2.2012.11.004, 2013.

1261   Melling, H., and Moore, R. M.: Modification of halocline source waters during freezing on the Beaufort

1262   Sea shelf: Evidence from oxygen isotopes and dissolved nutrients, Continental Shelf Research, 15,

1263   89-113, https://doi.org/10.1016/0278-4343(94)P1814-R, 1995.

1264   Menzel Barraqueta, J.-L., Schlosser, C., Planquette, H., Gourain, A., Cheize, M., Boutorh, J., Shelley,

1265   R., Contreira Pereira, L., Gledhill, M., Hopwood, M. J., Lacan, F., Lherminier, P., Sarthou, G., and

1266   Achterberg, E. P.: Aluminium in the North Atlantic Ocean and the Labrador Sea (GEOTRACES

1267   GA01 section): roles of continental inputs and biogenic particle removal, Biogeosciences, 15,

1268   5271–5286, https://doi.org/10.5194/bg-15-5271-2018, 2018. .

1269 Mercier, H., Lherminier, P., Sarafanov, A., Gaillard, F., Daniault, N., Desbruyères, D., Falina, A.,
1270   Ferron, B., Gourcuff, C., Huck, T., and Thierry, V.: Variability of the meridional overturning
1271   circulation at the Greenland–Portugal OVIDE section from 1993 to 2010, Progress in
1272   Oceanography, 132, 250-261, 10.1016/j.pocean.2013.11.001, 2015.
1273 Mil-Homens, M., Branco, V., Lopes, C., Vale, C., Abrantes, F., Boer, W., and Vicente, M.: Using factor
1274   analysis to charactierise historical trends of trace metal contamination in a sediment core from the
1275   Tagus Prodelta, Portugal, Water, Air, and Soil Pollution, 197, 277-287,
1276   https://doi.org/10.1007/s11270-008-9810-0, 2009.
1277 Moore, C. M., Mills, M. M., Langlois, R., Milne, A., Achterberg, E. P., La Roche, J., and Geider, R. J.:
1278   Relative influence of nitrogen and phosphorus availability on phytoplankton physiology and
1279   productivity in the oligotrophic sub-tropical North Atlantic Ocean, Limnology and Oceanography,
1280   53, 291-205, https://doi-org.inee.bib.cnrs.fr/10.4319/lo.2008.53.1.0291, 2008.
1281 Moore, C. M., Mills, M. M., Arrigo, K. R., Berman-Frank, I., Bopp, L., Boyd, P. W., Galbraith, E. D.,
1282   Geider, R. J., Guieu, C., Jaccard, S. L., Jickells, T. D., La Roche, J., Lenton, T. M., Mahowald, N.
1283   M., Marañón, E., Marinov, I., Moore, J. K., Nakatsuka, T., Oschlies, A., Saito, M. A., Thingstad, T.
1284   F., Tsuda, A., and Ulloa, O.: Processes and patterns of oceanic nutrient limitation, Nature
1285   Geoscience, 6, 701-710, 10.1038/ngeo1765, 2013.
1286 Moore, G. W. K.: Gale force winds over the Irminger Sea to the east of Cape Farewell, Greenland,
1287   Geophysical Research Letters, 30, 17, 10.1029/2003gl018012, 2003.
1288 Nielsdóttir, M. C., Moore, C. M., Sanders, R., Hinz, D. J., and Achterberg, E. P.: Iron limitation of the
1289   postbloom phytoplankton communities in the Iceland Basin, Global Biogeochemical Cycles,
1290   GB3001, doi:10.1029/2008GB003410, 2009.
1291 Olaffson, J., Thors, K., and Cann, J. R.: A sudden cruise off Iceland, RIDGE Events, 2, 35-28, 1991.
1292 Oschlies, A.: Nutrient supply to the surface waters of the North Atlantic: A model study, Journal of
1293   Geophysical Research, 107, 10.1029/2000jc000275, 2002.
1294 Painter, S. C., Henson, S. A., Forryan, A., Steigenberger, S., Klar, J., Stinchcombe, M. C., Rogan, N.,
1295   Baker, A. R., Achterberg, E. P., and Moore, C. M.: An assessment of the vertical diffusive flux of
1296   iron and other nutrients to the surface waters of the subpolar North Atlantic Ocean,
1297   Biogeosciences, 11, 2113-2130, 10.5194/bg-11-2113-2014, 2014.
1298 Palmer, M. R., Ludford, E. M., German, C. R., and Lilley, M. D.: Dissolved methane and hydrogen in
1299   the Steinahóll hydrothermal plume, 63°N, Reykjanes Ridge, in: Hydrothermal Vents and

1300   Processes, edited by: Parson, L. M., Walker, C. L., and Dixon, D. R., Special Publications,
1301   Geological Society, London, 111-120, 1995.

1302 Parekh, P., Follows, M. J., and Boyle, E. A.: Decoupling of iron and phosphate in the global ocean,
1303   Global Biogeochemical Cycle, 19, GB2020, https://doi-org.inee.bib.cnrs.fr/10.1029/2004GB002280,
1304   2005.

1305 Parra, M., Delmont, P., Ferragne, A., Latouche, C., Pons, J. C., and Puechmaille, C.: Origin and
1306   evolution of smectites in recent marine sediments of the NE Atlantic, Clay Minerals, 20, 335-346,
1307   https://doi.org/10.1180/claymin.1985.020.3.06, 1985.

1308 Pérez, F. F., Mercier, H., Vázquez-Rodríguez, M., Lherminier, P., Velo, A., Pardo, P. C., Rosón, G.,
1309   and Ríos, A. F.: Atlantic Ocean CO2 uptake reduced by weakening of the meridional overturning
1310   circulation, Nature Geoscience, 6, 146-152, 10.1038/ngeo1680, 2013.

1311 Pérez, F. F., Treguer, P., Branellec, P., García-Ibáñez, M. I., Lherminier, P., and Sarthou, G.: The
1312   2014 Greenland-Portugal GEOVIDE bottle data (GO-SHIP A25 and GEOTRACES GA01).
1313   SEANOE (Ed.), 2018.

1314 Petrich, C., and Eicken, H.: Growth, structure and properties of sea ice, in: Sea Ice. 2nd ed., edited by:
1315   Thomas, D. N., and Dieckmann, G. S., Wiley-Blackwell, Oxford, U.K., 23-77, 2010.

1316 Pickart, R. S., Straneo, F., and Moore, G. W. K.: Is Labrador Sea Water formed in the Irminger basin?,
1317   Deep Sea Research Part I:, 50, 23-52, https://doi.org/10.1016/S0967-0637(02)00134-6, 2003.

1318 Piron, A., Thierry, V., Mercier, H., and Caniaux, G.: Argo float observations of basin-scale deep
1319   convection in the Irminger sea during winter 2011–2012, Deep Sea Research Part I:
1320   Oceanographic Research Papers, 109, 76-90, 10.1016/j.dsr.2015.12.012, 2016.

1321 Radic, A., Lacan, F., and Murray, J. W.: Iron isotopes in the seawater of the equatorial Pacific Ocean:
1322   New constraints for the oceanic iron cycle, Earth and Planetary Science Letters, 306, 1-10,
1323   10.1016/j.epsl.2011.03.015, 2011.

1324 Ras, J., Claustre, H., and Uitz, J.: Spatial variability of phytoplankton pigment distribution in the
1325   Subtropical South Pacific Ocean: comparison between *in situ* and predicted data, Biogeosciences,
1326   5, 353-369, https://doi.org/10.5194/bg-5-353-2008, 2008.

1327 Riebesell, U., Schloss, I., and Smetacek, V.: Aggregation of algae released from melting sea ice:
1328   implications for seeding and sedimentation, Polar Biology, 11, 239-248,
1329   https://doi.org/10.1007/BF00238457, 1991.

1330   Rijkenberg, M. J., Middag, R., Laan, P., Gerringa, L. J., van Aken, H. M., Schoemann, V., de Jong, J.

1331   T., and de Baar, H. J.: The distribution of dissolved iron in the West Atlantic Ocean, PLoS One, 9,

1332   e101323, 10.1371/journal.pone.0101323, 2014.

1333   Sabine, C. L., Feely, R. A., Gruber, N., Key, R. M., Lee, K., Bullister, J. L., Wanninkhof, R., Wong, C.

1334   S., Wallace, D. W. R., Tilbrook, B., Millero, F. J., Peng, T.-H., Kozyr, A., Ono, T., and Rios, A. F.:

1335   The Oceanic sink for anthropogenic CO2, Science, 305, 367-371, 10.1126/science.1097403, 2004.

1336   Sanders, R., Brown, L., Henson, S., and Lucas, M.: New production in the Irminger Basin during 2002,

1337   Journal of Marine Systems, 55, 291-310, http:// dx.doi.org/10.1016/j.jmarsys.2004.09.002, 2005.

1338   Santos-Echeandia, J., Vale, C., Caetano, M., Pereira, P., and Prego, R.: Effect of tidal flooding on

1339   metal distribution in pore waters of marsh sediments and its transport to water column (Tagus

1340   estuary, Portugal), Mar Environ Res, 70, 358-367, 10.1016/j.marenvres.2010.07.003, 2010.

1341   Sarthou, G., and Jeandel, C.: Seasonal variations of iron concentrations in the Ligurian Sea and iron

1342   budget in the Western Mediterranean Sea, Marine Chemistry, 74, 115-129, 10.1016/s0304-

1343   4203(00)00119-5, 2001.

1344   Sarthou, G., Baker, A. R., Kramer, J., Laan, P., Laës, A., Ussher, S., Achterberg, E. P., de Baar, H. J.

1345   W., Timmermans, K. R., and Blain, S.: Influence of atmospheric inputs on the iron distribution in the

1346   subtropical North-East Atlantic Ocean, Marine Chemistry, 104, 186-202,

1347   10.1016/j.marchem.2006.11.004, 2007.

1348

1349   Sarthou, G., Laan, P., Ussher, S., Kramer, J., Timmermans, K. R. and Blain, S.: Influence of high

1350   atmospheric inputs on the iron distribution in the water column of the North Atlantic Ocean., 2003.

1351   Sarthou, G., Lherminier, P., Achterberg, E. P., Alonso-Pérez, F., Bucciarelli, E., Boutorh, J., Bouvier,

1352   V., Boyle, E. A., Branellec, P., Carracedo, L. I., Casacuberta, N., Castrillejo, M., Cheize, M.,

1353   Contreira Pereira, L., Cossa, D., Daniault, N., De Saint-Léger, E., Dehairs, F., Deng, F., Desprez

1354   de Gésincourt, F., Devesa, J., Foliot, L., Fonseca-Batista, D., Gallinari, M., García-Ibáñez, M. I.,

1355   Gourain, A., Grossteffan, E., Hamon, M., Heimbürger, L. E., Henderson, G. M., Jeandel, C.,

1356   Kermabon, C., Lacan, F., Le Bot, P., Le Goff, M., Le Roy, E., Lefèbvre, A., Leizour, S., Lemaitre,

1357   N., Masqué, P., Ménage, O., Menzel Barraqueta, J.-L., Mercier, H., Perault, F., Pérez, F. F.,

1358   Planquette, H. F., Planchon, F., Roukaerts, A., Sanial, V., Sauzède, R., Schmechtig, C., Shelley,

1359   R. U., Stewart, G., Sutton, J. N., Tang, Y., Tisnérat-Laborde, N., Tonnard, M., Tréguer, P., van

1360   Beek, P., Zurbrick, C. M., and Zunino, P.: Introduction to the French GEOTRACES North Atlantic

1361   Transect (GA01): GEOVIDE cruise, Biogeosciences, 15, 7097–7109, https://doi.org/10.5194/bg-

1362   15-7097-2018, 2018.

1363

1364   Sarthou, G., Vincent, D., Christaki, U., Obernosterer, I., Timmermans, K. R., and Brussaard, C. P. D.:

1365   The fate of biogenic iron during a phytoplankton bloom induced by natural fertilisation: Impact of

1366   copepod grazing, Deep Sea Research Part II: Topical Studies in Oceanography, 55, 734-751,

1367   10.1016/j.dsr2.2007.12.033, 2008.

1368   Ocean Data View, https://odv.awi.de ODV4, version 4.7.6 (23 March 2016), access: 6 April, 2016.

1369   Schmidt, S. and Reyss, J.-L.: Radium as internal tracer of Mediterranean Outflow Water, Journal of

1370   Geophysical Research, 101, 3589–3596, 1996.

1371   Schroth, A. W., Crusius, J., Hoyer, I., and Campbell, R.: Estuarine removal of glacial iron and

1372   implications for iron fluxes to the ocean, Geophysical Research Letters, 41, 3951-3958,

1373   10.1002/2014GL060199, 2014.

1374   Shelley, R. U., Morton, P. L., and Landing, W. M.: Elemental ratios and enrichment factors in aerosols

1375   from the US-GEOTRACES North Atlantic transects, Deep Sea Research, 116, 262-272,

1376   https://doi.org/10.1016/j.dsr2.2014.12.005, 2015.

1377   Shelley, R. U., Roca-Martí, M., Castrillejo, M., Sanial, V., Masqué, P., Landing, W. M., van Beek, P.,

1378   Planquette, H., and Sarthou, G.: Quantification of trace element atmospheric deposition fluxes to

1379   the Atlantic Ocean (>40°N; GEOVIDE, GEOTRACES GA01) during spring 2014, Deep Sea

1380   Research Part I: Oceanographic Research Papers, 119, 34-49, 10.1016/j.dsr.2016.11.010, 2017.

1381   Shelley, R. U., Landing, W. M., Ussher, S. J., Planquette, H., and Sarthou, G.: Regional trends in the

1382   fractional solubility of Fe and other metals from North Atlantic aerosols (GEOTRACES cruises

1383   GA01 and GA03) following a two-stage leach, Biogeosciences, 15, 2271–2288,

1384   https://doi.org/10.5194/bg-15-2271-2018, 2018.

1385   Shor, A., Lonsdale, P., Hollister, D., and Spencer, D.: Charlie-Gibbs fracture zone: bottom-water

1386   transport and its geological effects, Deep Sea Research, 27A, 325-345,

1387   https://doi.org/10.1016/0198-0149(80)90030-8, 1980.

1388   Sinha, M. C., Navin, D. A., MacGregor, L. M., Constable, S., Peirce, C., White, A., Heinson, G., and

1389   Inglis, M. A.: Evidence for accumulated melt beneath the slow-spreading Mid-Atlantic Ridge,

1390   Philosophical Transactions of the Royal Society A, 355, 233-253,

1391   https://doi.org/10.1098/rsta.1997.0008, 1997.

1392   Slagter, H. A., Reader, H. E., Rijkenberg, M. J. A., Rutgers van der Loeff, M., de Baar, H. J. W., and
1393   Gerringa, L. J. A.: Organic Fe speciation in the Eurasian Basins of the Arctic Ocean and its relation
1394   to terrestrial DOM, Marine Chemistry, 197, 11-25, 10.1016/j.marchem.2017.10.005, 2017.

1395   Smallwood, J. R., and White, R. S.: Crustal accretion at the Reykjanes Ridge, 61°-62°N, Journal of
1396   Geophysical Research: Solid Earth, 103, 5185-5201, 10.1029/97jb03387, 1998.

1397   Statham, P. J., Skidmore, M., and Tranter, M.: Inputs of glacially derived dissolved and colloidal iron to
1398   the coastal ocean and implications for primary productivity, Global Biogeochemical Cycles, 22, 1-
1399   11, 10.1029/2007GB003106, 2008.

1400   Sunda, W. G., and Huntsman, S. A.: Iron uptake and growth limitation in oceanic and coastal
1401   phytoplankton, Marine Chemistry, 50, 189-206, 10.1016/0304-4203(95)00035-p, 1995.

1402   Sutherland, D. A., Pickart, R. S., Peter Jones, E., Azetsu-Scott, K., Jane Eert, A., and Ólafsson, J.:
1403   Freshwater composition of the waters off southeast Greenland and their link to the Arctic Ocean,
1404   Journal of Geophysical Research, 114, 10.1029/2008jc004808, 2009.

1405   Tagliabue, A., Aumont, O., DeAth, R., Dunne, J. P., Dutkiewicz, S., Galbraith, E., Misumi, K., Moore,
1406   J. K., Ridgwell, A., Sherman, E., Stock, C., Vichi, M., Völker, C. and Yool, A.: How well do global
1407   ocean biogeochemistry models simulate dissolved iron distributions?, Global Biogeochemical
1408   Cycles, 30(2), 149–174, doi:10.1002/2015GB005289, 2016.

1409   Tanhua, T., Olsson, K. A., and Jeansson, E.: Formation of Denmark Strait overflow water and its
1410   hydro-chemical composition, Journal of Marine Systems, 57, 264-288,
1411   10.1016/j.jmarsys.2005.05.003, 2005.

1412   Teng, Z., Huang, J. Y., Fujito, K., and Takizawa, S.: Manganese removal by hollow fiber micro-
1413   filter.Membrane separation for drinking water, Euroopean Conference on Desalination and the
1414   Environment, Amsterdam, 28 May, 2001.

1415   Thuróczy, C. E., Gerringa, L. J. A., Klunder, M. B., Middag, R., Laan, P., Timmermans, K. R., and de
1416   Baar, H. J. W.: Speciation of Fe in the Eastern North Atlantic Ocean, Deep Sea Research Part I:
1417   Oceanographic Research Papers, 57, 1444-1453, 10.1016/j.dsr.2010.08.004, 2010.

1418   Tonnard, M., Donval, A., Lampert, L., Tréguer, P., Bowie, A. R., van der Merwe, P., planquette, H.,
1419   Claustre, H., Dimier, C., Ras, J., and Sarthou, G.: Phytoplankton assemblages in the North Atlantic
1420   Ocean and in the Labrador Sea along the GEOVIDE section (GEOTRACES section GA01)
1421   determined by CHEMTAX analysis from HPLC pigment data, Biogeosciences, in prep.

1422 Tovar-Sanchez, A., Duarte, C. M., Alonso, J. C., Lacorte, S., Tauler, R., and Galban-Malagon, C.:
1423   Impacts of metals and nutrients released from melting multiyear Arctic sea ice, Journal of
1424   Geophysical Research-Oceans, 115, 10.1029/2009jc005685, 2010.

1425 Tréguer, P. J., and De La Rocha, C. L.: The world ocean silica cycle, Ann Rev Mar Sci, 5, 477-501,
1426   10.1146/annurev-marine-121211-172346, 2013.

1427 Twining, B. S., Baines, S. B., Fisher, N. S., and Landry, M. R.: Cellular iron contents of plankton during
1428   the Southern Ocean Iron Experiment (SOFeX), Deep Sea Research Part I: Oceanographic
1429   Research Papers, 51, 1827-1850, 10.1016/j.dsr.2004.08.007, 2004.

1430 Van Beusekom, J. E. E.: Distribution of aluminium in surface waters of the North Sea: influence of
1431   suspended matter., in: Biogeochemistry and Distribution of Suspended Matter in the North Sea and
1432   Implications to fisheries Biology, edited by: Kempe, S., Mittleitungen aus dem Geologisch-
1433   Paläontologischen Institut der Universität Hamburg, SCOPE/UNEP Sonderband, 117-136, 1988.

1434 von Appen, W.-J., Koszalka, I. M., Pickart, R. S., Haine, T. W. N., Mastropole, D., Magaldi, M. G.,
1435   Valdimarsson, H., Girton, J., Jochumsen, K., and Krahmann, G.: The East Greenland Spill Jet as
1436   an important component of the Atlantic Meridional Overturning Circulation, Deep Sea Research
1437   Part I: Oceanographic Research Papers, 92, 75-84, 10.1016/j.dsr.2014.06.002, 2014.

1438 Wadhams, P.: Ice in the Ocean, Gordon and Breach Science Publishers, London, UK, 2000.

1439 Wagener, T., Guieu, C., and Leblond, N.: Effects of dust deposition on iron cycle in the surface
1440   Mediterranean Sea: results from a mesocosm seeding experiment, Biogeosciences, 7, 3769–3781,
1441   https://doi.org/10.5194/bg-7-3769-2010, 2010. .

1442 Woodgate, R. A., and Aagaard, K.: Revising the Bering Strait freshwater flux into the Arctic Ocean,
1443   Geophysical Research Letters, 32, 10.1029/2004GL021747., 2005.

1444 Wuttig, K., Wagener, T., Bressac, M., Dammshäuser, A., Streu, P., Guieu, C., and Croot, P. L.:
1445   Impacts of dust deposition on dissolved trace metal concentrations (Mn, Al and Fe) during a
1446   mesocosm experiment, Biogeosciences, 10, 2583-2600, 10.5194/bg-10-2583-2013, 2013.

1447 Yashayaev, I., Bersch, M. and Aken, H. M. van: Spreading of the Labrador Sea Water to the Irminger
1448   and Iceland basins, Geophysical Research Letters, 34(10), doi:10.1029/2006GL028999, 2007.

1449 Zou, S., Lozier, S., Zenk, W., Bower, A., and Johns, W.: Observed and modeled pathways of the
1450   Iceland Scotland Overflow Water in the eastern North Atlantic, Progress in Oceanography, 159,
1451   211-222, 10.1016/j.pocean.2017.10.003, 2017.

1452   Zunino, P., Lherminier, P., Mercier, H., Daniault, N., García-Ibáñez, M. I., and Pérez, F. F.: The

1453   GEOVIDE cruise in May–June 2014 reveals an intense Meridional Overturning Circulation over a

1454   cold and fresh subpolar North Atlantic, Biogeosciences, 14, 5323–5342, https://doi.org/10.5194/bg-

1455   14-5323-2017, 2017.

1456

1457

1458 **Figure 1: Map of the GEOTRACES GA01 voyage plotted on bathymetry as well as the major topographical**
1459 **features and main basins. Crossover station with GEOTRACES voyage (GA03) is shown as a red star.**
1460 **(Ocean Data View (ODV) software, version 4.7.6, R. Schlitzer, http://odv.awi.de, 2016). BFZ: Bight Fracture**
1461 **Zone, CGFZ: Charlie-Gibbs Fracture Zone.**

1462
1463
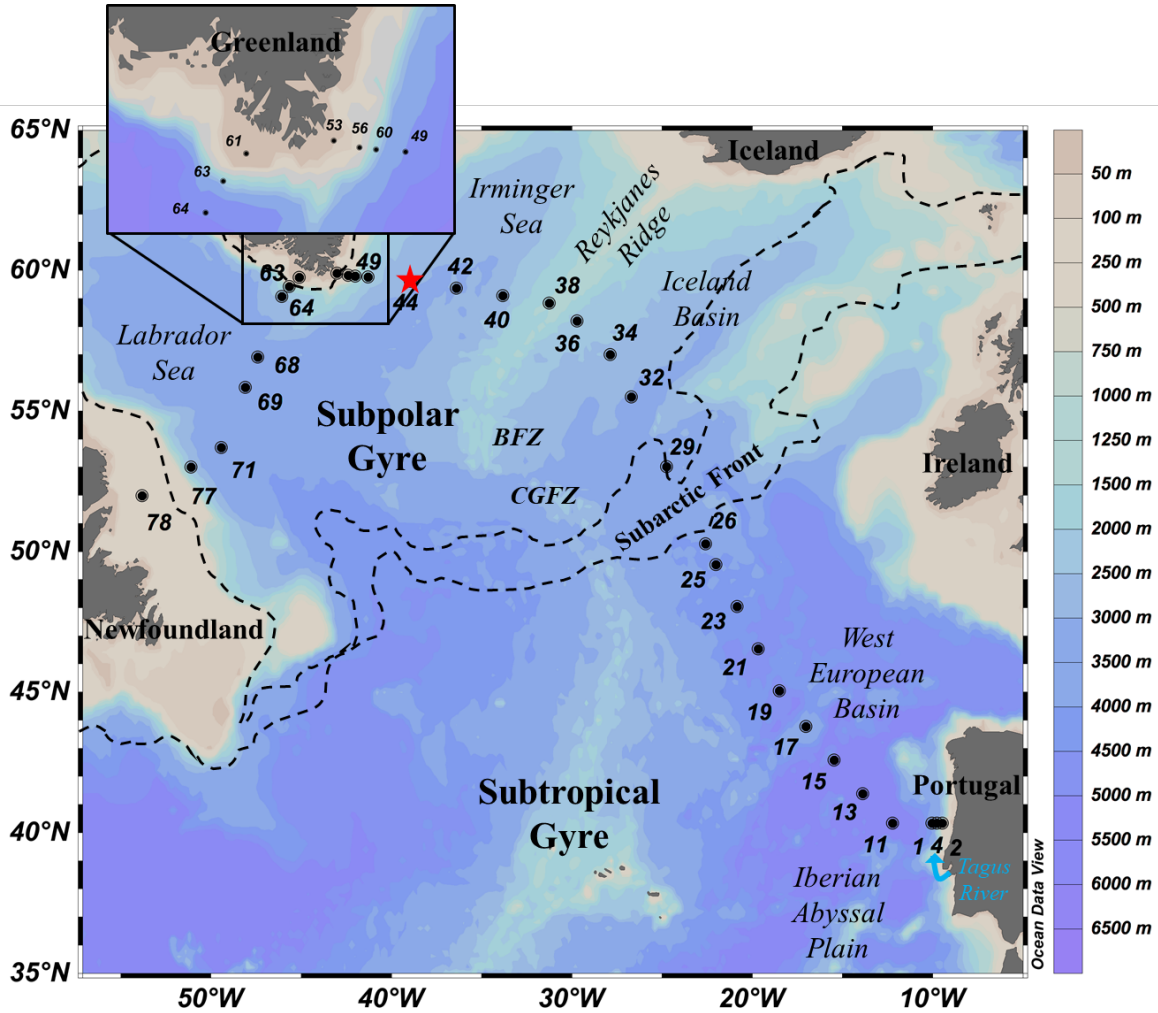
1464
1465

1466 **Figure 2: Parameters measured from the regular CTD cast represented as a function of depth for GA01**
1467 **section for (A) Dissolved Oxygen (O_2, µmol kg^{-1}), (B) Salinity and (C) Temperature (°C). The contour lines**
1468 **represent isopycnals (neutral density, γ^n, in units of kg m^{-3}).**
1469
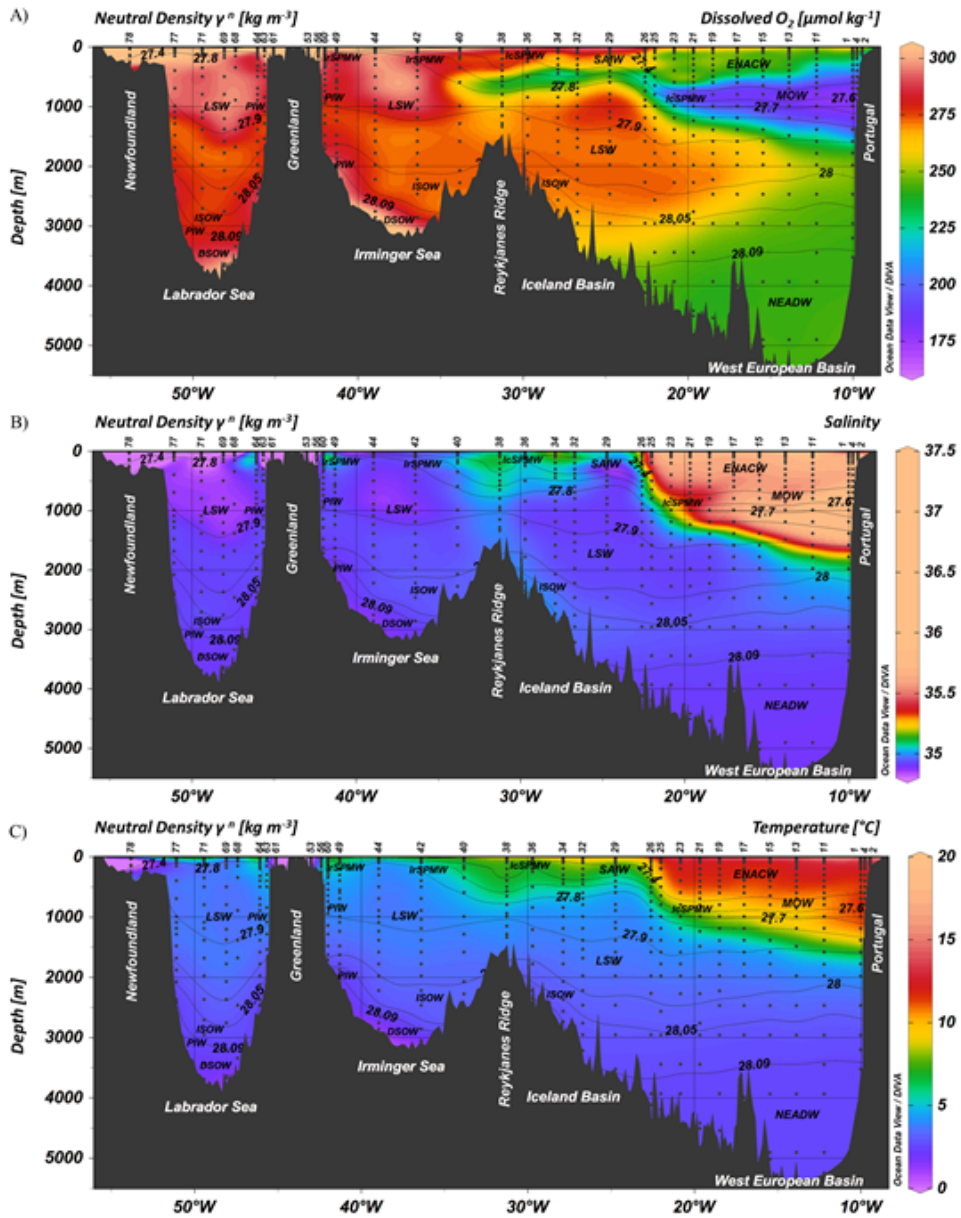
Surface water masses

|	
ENACW	East North Atlantic Central Water
IcSPMW	Iceland SubPolar Mode Water
IrSPMW	Irminger SubPolar Mode Water
SAIW	Subarctic Intermediate Water

Intermediate water masses

MOW	Mediterranean Outflow Water
LSW	Labrador Sea Water

Overflow Deep water masses

NEADW	North East Atlantic Deep Water
PIW	Polar Intermediate Water
ISOW	Iceland-Scotland Overflow Water
DSOW	Denmark Strait Overflow Water

1470

Figure 3: Contour plot of the distribution of dissolved iron (DFe) concentrations in nmol L^{-1} along the GA01 voyage transect: upper 1000 m (top) and full depth range (bottom). The red dashed line indicates the depth of the Surface Mixed Layer (SML). Small black dots represent collected water samples at each sampling station. (Ocean Data View (ODV) software, version 4.7.6, R. Schlitzer, http://odv.awi.de, 2016).
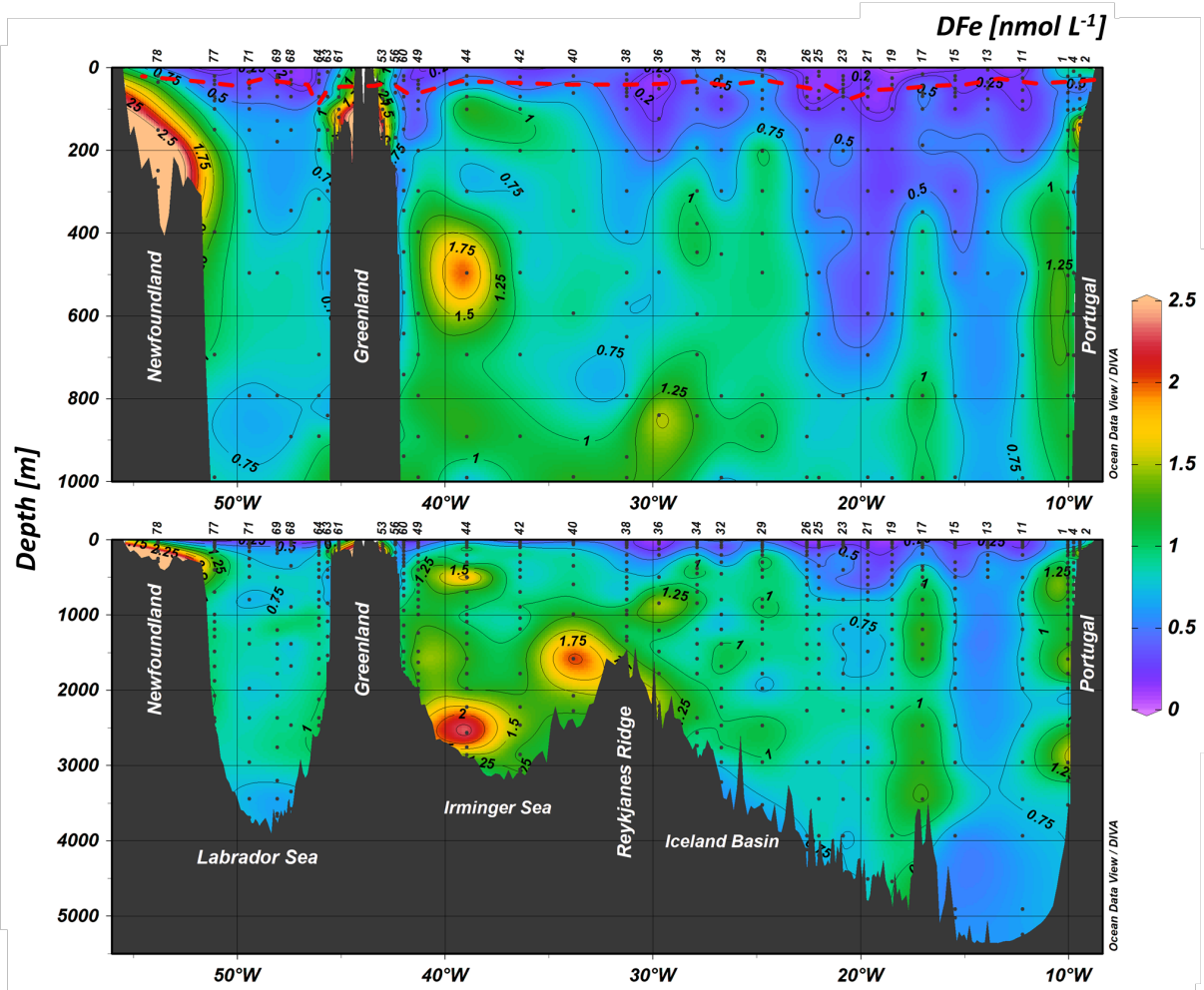
Figure 4: Vertical profiles of dissolved iron (DFe, black dots, solid line), particulate iron (PFe, black open dots, dashed line, Gourain et al., 2019) and dissolved aluminium (DAl, grey dots, Menzel Barraqueta et al., 2018) at Stations 2 (A), and 4 (B) located above the Iberian shelf, Station 56 (C), Stations 53 (D) 53 and Station 61 (E) located above the Greenland shelf and Station 78 (F) located above the Newfoundland shelf. Note that for stations 53, 61 and 78, plots of the percentage of meteoric water (open dots) and sea-ice melting (black dots and dashed line) (Benetti et al., see text for details), Total Chlorophyll-*a* (TChl-*a*, green), temperature (blue) and salinity (black) are also displayed as a function of depth.

14.9
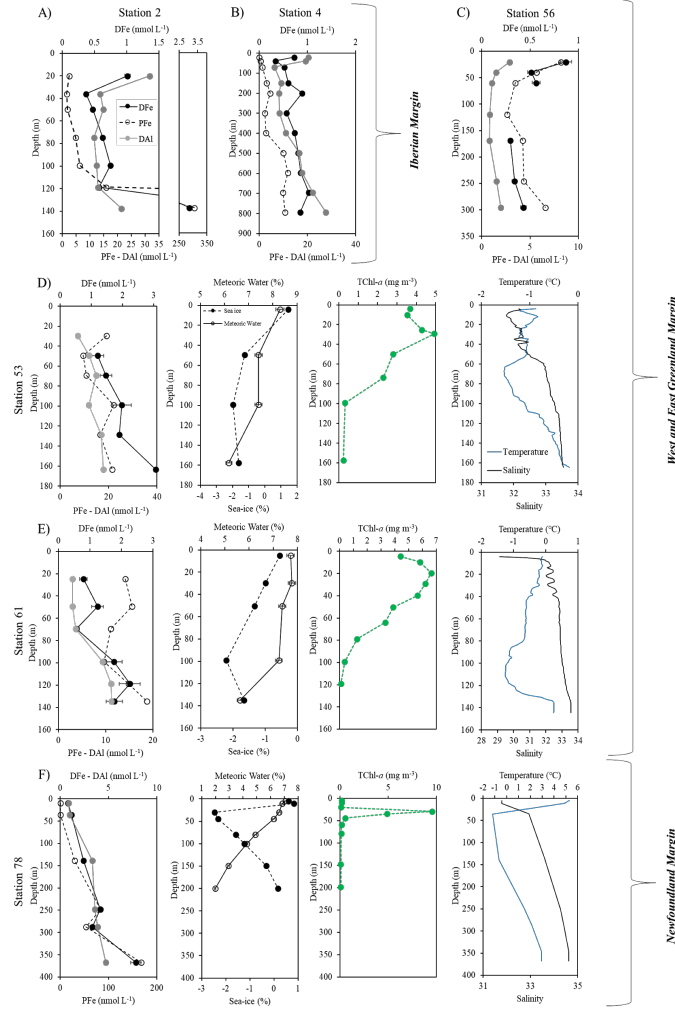
Figure 5: Plot of dissolved iron (DFe, black circles) and dissolved aluminium (DAl, white circles, Menzel
Barraqueta et al., 2018) at ~ 20 m, along the salinity gradient between stations 1, 2, 4, and 11 with linear
regression equations. Numbers close to sample points representing station numbers.

1498

1499

1500

1501

1502

1503

1504
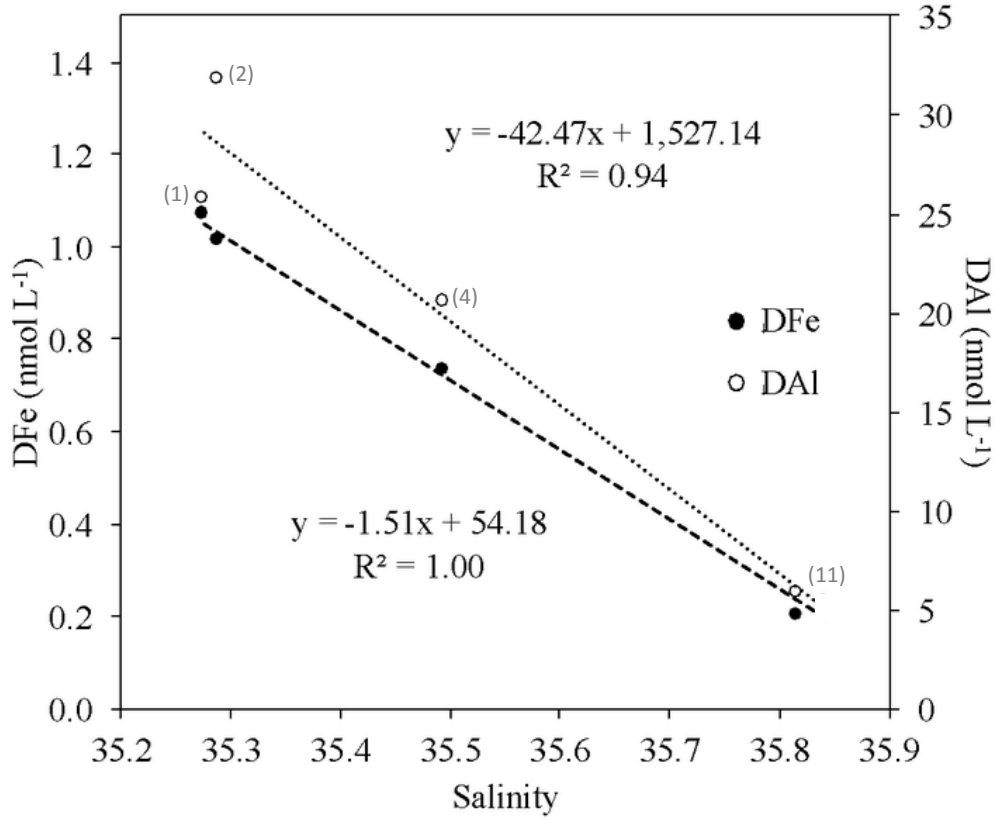
Figure 6: Plot of dissolved Fe (DFe) Turnover Times relative to Atmospheric Deposition (TTADs) calculated from soluble Fe contained in aerosols estimated from a two-stage sequential leach (UHP water, then 25% HAc, Shelley et al., this issue). Note that numbers on top of points represent station numbers and that the colour coding refers to different region with in yellow, margin stations; in purple, the West European Basin; in blue, the Iceland Basin; in green, the Irminger Sea and in red, the Labrador Sea. The numbers on top of the plot represent TTADs averaged for each oceanic basin and their standard deviation.
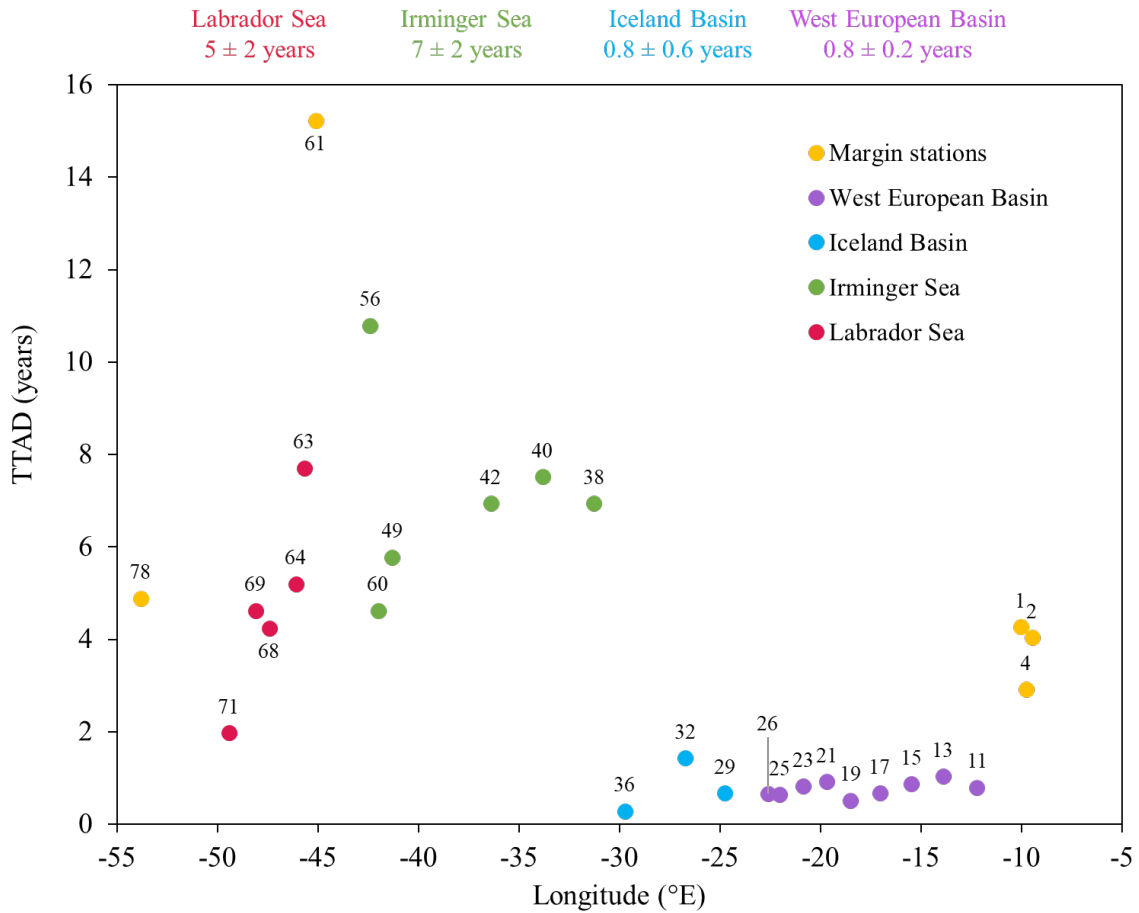
Figure 7: Section plot of the Fe* tracer in the North Atlantic Ocean with a remineralization rate ($R_{Fe:N}$) of 0.05 mmol mol^{-1} from surface to 225 m depth. A contour line of 0 separates areas of negative Fe* from areas with positive Fe*. Positive values of Fe* imply there is enough iron to support complete consumption of NO_3^- when this water is brought to surface, and negative Fe* values imply a deficit. See text for details.
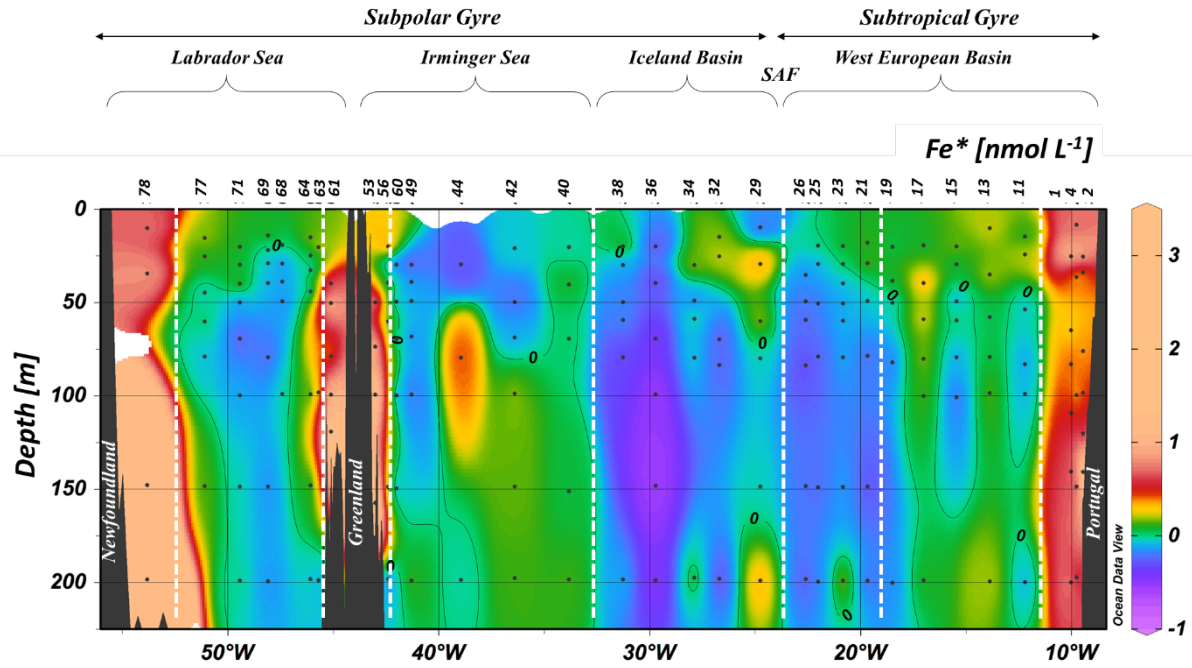
1522

1523 Table 1: Station number, date of sampling (in the DD/MM/YYYY format), size pore used for filtration
1524 (μm), station location, mixed layer depth (m) and associated average dissolved iron (DFe)
1525 concentrations, standard deviation and number of samples during the GEOTRACES GA01 transect.
1526 Note that the asterisk next to station numbers refers to disturbed temperature and salinity profiles as
1527 opposed to uniform profiles.

Station	Date sampling	filtration	Latitude	Longitude	Z_m	DFe (nmol L^{-1})		
	DD/MM/YYYY	μm	°N	°E	m	average	SD	n
1	19/05/2014	0.2	40.33	-10.04	25.8	1.07 ±	0.12	1
2	21/05/2014	0.2	40.33	-9.46	22.5	1.01 ±	0.04	1
4	21/05/2014	0.2	40.33	-9.77	24.2	0.73 ±	0.03	1
11	23/05/2014	0.2	40.33	-12.22	31.3	0.20 ±	0.11	2
13	24/05/2014	0.45	41.38	-13.89	18.8	0.23 ±	0.02	1
15	28/05/2014	0.2	42.58	-15.46	34.2	0.22 ±	0.03	2
17	29/05/2014	0.2	43.78	-17.03	36.2	0.17 ±	0.01	1
19*	30/05/2014	0.45	45.05	-18.51	44.0	0.13 ±	0.05	2
21	31/05/2014	0.2	46.54	-19.67	47.4	0.23 ±	0.08	2
23*	02/06/2014	0.2	48.04	-20.85	69.5	0.21 ±	0.05	6
25	03/06/2014	0.2	49.53	-22.02	34.3	0.17 ±	0.04	2
26	04/06/2014	0.45	50.28	-22.60	43.8	0.17 ±	0.03	2
29	06/06/2014	0.45	53.02	-24.75	23.8	0.17 ±	0.02	1
32	07/06/2014	0.2	55.51	-26.71	34.8	0.59 ±	0.08	2
34	09/06/2014	0.45	57.00	-27.88	25.6	NA ±		0

36	10/06/2014	0.45	58.21	-29.72	33.0	0.12	±	0.02	1
38	10/06/2014	0.45	58.84	-31.27	34.5	0.36	±	0.16	2
40	12/06/2014	0.45	59.10	-33.83	34.3	0.39	± P	0.05	1
42	12/06/2014	0.45	59.36	-36.40	29.6	0.36	±	0.05	1
44	13/06/2014	0.2	59.62	-38.95	25.8	NA	±		0
49	15/06/2014	0.45	59.77	-41.30	60.3	0.30	±	0.05	2
53*	17/06/2014	0.45	59.90	-43.00	36.4	NA	±		0
56*	17/06/2014	0.45	59.82	-42.40	30.0	0.87	±	0.06	1
60*	17/06/2014	0.45	59.80	-42.00	36.6	0.24	±	0.02	2
61*	19/06/2014	0.45	59.75	-45.11	39.8	0.79	±	0.12	1
63*	19/06/2014	0.45	59.43	-45.67	86.7	0.40	±	0.03	1
64	20/06/2014	0.45	59.07	-46.09	33.9	0.27	±	0.06	2
68*	21/06/2014	0.45	56.91	-47.42	26.3	0.22	±	0.01	1
69*	22/06/2014	0.45	55.84	-48.09	17.5	0.24	±	0.02	1
71	24/06/2014	0.45	53.69	-49.43	36.7	0.32	±	0.04	2
77*	26/06/2014	0.45	53.00	-51.10	26.1	NA	±		0
78	27/06/2014	0.45	51.99	-53.82	13.4	0.79	±	0.05	1

1528
1529
1530
1531
1532
1533

Table 2: SAFe S, GSP and NASS-7 dissolved iron concentrations (DFe, nmol L-1) determined by the SeaFAST-picoTM and their consensus (SAFe S, GSP; https://websites.pmc.ucsc.edu/~kbruland/GeotracesSaFe/kwbGeotracesSaFe.html) and certified (NASS-7; https://www.nrc-cnrc.gc.ca/eng/solutions/advisory/crm/certificates/nass_7.html) DFe concentrations. Note that yet no consensual value is reported for the GSP seawater.

Seawater used for calibration	Sea*FAST*-pico[TM] DFe values (nmol L^{-1})				reference or certified DFe values (nmol L^{-1})		
	Average		SD	n	Average		SD
SAFe S	0.100	±	0.006	2	0.095	±	0.008
GSP	0.16	±	0.04	15	NA	±	NA
NASS-7	6.7	±	1.7	12	6.3	±	0.5

1557 Table 3: Averaged DFe:DAl (Menzel Barraqueta et al., 2018) and PFe:PAl (Gourain et al., in
1558 prep.2019) ratios reported per margins. Note that to avoid phytoplankton uptake, only depth below 100
1559 m depth are considered.

1560

Margins	Stations	DFe:DAl (mol:mol)		PFe:PAl (mol:mol)		DFe:PFe (mol:mol)			n
	#	average	SD	average	SD	average		SD	
Iberian Margin	2 and 4	0.07 ±	0.03	0.20 ±	0.01	0.13	±	0.09	10
East Greenland Margin	56 and 53	0.21 ±	0.09	0.30 ±	0.01	0.12	±	0.03	6
West Greenland Margin	61	0.18 ±	0.02	0.32 ±	0.01	0.14	±	0.04	3
Newfoundland Margin	78	1.1 ±	0.41	0.31 ±	0.01	0.06	±	0.02	4

1561
1562